

Transition from no-ELM response to pellet ELM triggering during pedestal build-up – insights from extended MHD simulations

S Futatani¹, A Cathey^{2,3}, M Hoelzl², P T Lang², G T A Huijsmans^{4,5}, M. Dunne², JOREK Team⁶, ASDEX Upgrade Team⁷, and EUROfusion MST1 Team⁸

¹Universitat Politècnica de Catalunya, Barcelona, Spain

²Max Planck Institute for Plasma Physics, Boltzmannstr. 2, 85748 Garching b. M., Germany

³Physik Department, E28, TUM, 85748 Garching, Germany

⁴CEA, IRFM, 13108 Saint-Paul-Lez-Durance, France

⁵Eindhoven University of Technology, P.O. Box 513, 5600 MB Eindhoven, The Netherlands

⁶refer to [M Hoelzl, G T A Huijsmans, S J P Pamela, M Becoulet, E Nardon, F J Artola, B Nkonga et al, Nuclear Fusion, in preparation] for a list of team members

⁶see the author list of [H. Meyer et al. 2019 Nucl. Fusion 59 112014]

⁷see the author list of [B. Labit et al. 2019 Nucl. Fusion 59 0860020]

Abstract

Pellet ELM triggering is a well established scheme for decreasing the time between two successive ELM crashes below its natural value. Reliable ELM pacing has been demonstrated experimentally in several devices increasing the ELM frequency considerably. However, it was also shown that the frequency cannot be increased arbitrarily due to a so-called lag-time. During this time after a preceding natural or triggered ELM crash, neither a natural ELM crash occurs nor the triggering of an ELM crash by pellet injection is possible. For this article, pellet ELM triggering simulations are advanced beyond previous studies in two ways. Firstly, realistic ExB and diamagnetic background flows are included. And secondly, the pellet is injected at different stages of the pedestal build-up. This allows to recover the lag-time for the first time in simulations and investigate it in detail. A series of non-linear extended MHD simulations is performed to investigate the plasma dynamics resulting from an injection at different time points during the pedestal build-up. The experimentally observed lag-time is qualitatively reproduced well. In particular, a sharp transition is observed between the regime where no ELMs can be triggered and the regime where pellet injection causes an ELM crash. Via variations of pellet parameters and injection time, the two regimes are studied and compared in detail revealing pronounced differences in the non-linear dynamics. The toroidal mode spectrum is significantly broader when an ELM crash is triggered enhancing the stochasticity and therefore also the losses of thermal energy along magnetic field lines. In the heat fluxes to the divertor targets, pronounced toroidal asymmetries are observed. In case of high injection velocities leading to deep penetration, also the excitation of core modes like the 2/1 neoclassical tearing mode is observed.

1 Introduction

1.1 Motivation

Type-I edge localized modes (ELMs) show an unfavorable scaling towards large machines like ITER both regarding thermal energy losses and the wetted area across which heat loads are distributed at the divertor targets [1] such that ELM control is essential. The application of external resonant magnetic perturbation fields (RMPs) is a promising approach [2], however the applicability was often found to be restricted to particular “windows” in the edge safety factor q_{95} . Contrary to existing tokamaks, ITER is expected to be in ELMy H-mode also during ramp-up and ramp-down. The RMP operational windows may not allow reliable control in these phases because q_{95} is evolving during the transient periods. Pellet ELM triggering offers a complementary approach, allowing to increase the ELM frequency and reduce ELM losses [3–5]. It is imperative to investigate the lag time after a preceding ELM crash during which ELM triggering by pellets is not possible, since it poses an upper limit for the maximum achievable ELM frequency [6]. In the present article, pellet ELM triggering simulations are improved beyond the state of the art, e.g., by including realistic plasma background flows, by studying the injection at various time points during pedestal build-up. This way, the lag time and the transition from a regime where ELM triggering is not possible early in the pedestal build-up into the ELM triggering regime is studied in simulations for the first time. The non-linear features of both regimes are studied and compared in detail.

The article is structured as follows. Within the present Section 1, a brief overview is given of the experimental background for pellet ELM triggering (Subsection 1.2) and information is given on previous simulations (Subsection 1.3). Section 2 explains the simulation setup used for the present study. The actual simulation results are presented and analyzed in the following Sections. First, at constant pellet size and constant injection velocity, the time of injection during the pedestal build-up is varied in Section 3, to investigate the transition from no-ELM into the ELM triggering regime. The influence of the injected pellet size onto this transition is further investigated in Section 4. Based on these results, the no-ELM and ELM triggering regimes are compared in depth in Section 5 to highlight key differences in the plasma response. The influence of the injection velocity onto the plasma response is analyzed via an additional parameter scan in Section 6. Finally, conclusions and an outlook are provided in Section 7. References and Acknowledgements follow at the very end of the article.

1.2 Experimental background

At ASDEX Upgrade in the divertor DIV IIB [7] configuration and a vessel wall surface covered with about half of carbon and half tungsten-coated (AUG-C), first pioneering experiments on ELM pacing and mitigation by pellet injection were performed [3]. For cases where the pellet injection rate $f_p > 1.5 \times f_{\text{ELM}}^0$ with f_{ELM}^0 the natural ELM frequency, full ELM frequency control with $f_{\text{ELM}} = f_p$ was achieved [3, 8]. Furthermore, albeit only with f_{ELM} in the range 50 – 110 Hz, $dW_{\text{ELM}}/W_0 \sim 1/f_{\text{ELM}}$ was found, with

dW_{ELM} the ELM induced plasma energy loss and W_0 the pre-ELM plasma energy [7]. However, at high pellet injection frequencies, unwanted increases of the plasma density were observed [6]. For the investigated experimental conditions, every pellet injected during an H-mode phase triggered an ELM within less than 0.3 ms after reaching the separatrix [9]. Main findings of AUG-C were confirmed at other machines like DIII-D [10] and JET [11]. In DIII-D, small pellets (1.3 mm cylindrical pellet) triggered small ELMs within 0.1 ms of the pellet entering the plasma [5]. The ELM event is found within 1 cm of the pellet crossing the separatrix, while slightly shallower than what is observed in AUG-C, 3 cm [12]. Spontaneous and triggered ELMs were shown to have very similar properties [13]. Motivated by these findings, ELM control by pellets was re-visited in the tungsten ASDEX Upgrade configuration (AUG-W) [6]. A dedicated analysis of a specific plasma scenario showed that successful ELM triggering entails a lag time. During such lag time, injected pellets fail to trigger an ELM crash. This poses an upper limit on the achievable ELM pacing frequency. The lag time did not show clear correlations to the imposed magnitude of the pellet perturbation, i.e. different pellet sizes or velocities. However, under different plasma conditions, cases were found with pellets failing to trigger ELMs although the pedestal had almost fully recovered from the previous ELM crash. On the other hand, sometimes another ELM was initiated very shortly after an ELM with yet the energy drop still present. This indicates that pedestal stability is not monotonically decreasing over the ELM cycle. The observation of pellet-triggered ELMs without a pronounced pedestal was repeated in attempts to achieve ELM control at the L-H transition by means of pellet pacing both in the AUG-W and JET all-metal-wall tokamaks [14].

1.3 Previous simulations

Theoretical and numerical approaches to understand the non-linear MHD physics in response to a pellet injection is a high priority research topic. There are extensively elaborated extended non-linear MHD codes world wide such as NIMROD [15], M3D-C1 [16], BOUT++ [17], JOEKE [18] in order to understand the physics in realistic geometry. The physics of edge localized modes (ELMs) and ELM control by RMPs, QH-mode (Quiescent H-mode), vertical magnetic kicks, and pellets was investigated already via non-linear simulations in many ways using the JOEKE code [18–24]. Very recently, type-I ELM cycles and the triggering mechanism responsible for the violent onset of the ELM crash were studied for the first time [25]. These ELM cycle simulations form the basis for investigating pellet injection at various times during the inter-ELM phase in the present article. The injection of pellets into ASDEX Upgrade for ELM triggering had not been simulated before. However, the injection of deuterium shattered pellets for disruption mitigation was already studied using similar physics models like they are applied in the present article [20]. The injection of pellets for ELM control has also been studied with M3D-C1; for hydrogenic pellets [26] and for Lithium Granule Injection in linear simulations [27]. Further work in particular on impurity pellet injection exists, but is aiming at disruption mitigation. First simulations using JOEKE for the triggering of an ELM crash by the injection of a frozen deuterium pellet modelled as a

localized, static density perturbation were shown in Ref. [28]. Afterwards, results based on a spatio-temporally varying pellet ablation model were shown including experimental comparisons to DIII-D [24] and JET [29]. The pellet size requirement for ELM triggering in the stable plasma was found to be $\sim 70\%$ of the minimum pedestal pressure which causes spontaneous ELM. The key parameter of ELM control by pellet injection is the three-dimensionally localized pressure perturbation at the plasma edge, and the physics understanding is continued to be revealed by theory and numerical simulations [24, 28]. In experiments, pellets can be only launched at certain time slots, therefore the timing of pellets reaching the plasma is difficult to choose. In the study of pellet-triggered ELMs in JET, the pellets were injected into the unstable plasma slightly before the spontaneous ELM event. The JOREK simulations showed good agreement with the experimental observations of the heat flux reaching the plasma facing components (PFC), $\sim 60 \text{ MW/m}^2$ [30]. The magnitude of the peak of the heat flux is similar between the spontaneous ELM and the pellet-triggered ELM, also consistent with the experiment. Furthermore, a toroidally asymmetric heat deposition onto the divertor targets related to pellet-triggered ELMs has been observed in the previous simulations for DIII-D and JET [24, 29] consistent with experimental observations [31].

This article extends previous work in several ways. The first pellet ELM triggering simulations are presented for ASDEX Upgrade, realistic ExB and diamagnetic background flows are included for the first time, and the injection during different phases of pedestal build-up is studied for the first time. This allows detailed insights into the experimentally observed lag-time. A direct comparison between simulations of spontaneous and pellet-triggered ELMs is not part of this work, but is studied separately in [32].

2 Simulation setup

Pellet ELM pacing experiments in the ASDEX Upgrade tokamak [33] are performed using a system which injects pellets from top of the High Field Side (HFS) as shown in Ref. [6]. Pellets are prepared in the cryogenic system and transported to the HFS via a 17 meter long guiding tube. The technical capabilities of the pellet injector at ASDEX Upgrade are the following: an injection frequency up to 70 Hz is possible, the pellet size can range from 1.5×10^{20} to 3.7×10^{20} [particles/pellet], and the injection velocity can range between 240 and 1040 m/s (dependent on the pellet size). In the simulations, the pellet size is the number of atoms contained in a pellet. For example, ' $0.8 \times 10^{20}\text{D}$ ' is a pellet which contains 0.8×10^{20} deuterium atoms. In the simulations, the initial pellet location is $R = 1.365 \text{ [m]}$, $Z = 0.6737 \text{ [m]}$ where the normalized poloidal magnetic flux of $\Psi_N = 1.019$. It corresponds to 1.8 cm outside the separatrix as shown in Fig 1.

We assume that about 50 % of the pellet particles are lost in the 17 m long pellet guide such that our base simulations carried out with pellets containing 0.8×10^{20} Deuterium atoms correspond approximately to the smallest pellet size possible experimentally. In addition, simulations with 0.4×10^{20} and 1.5×10^{20} atoms are carried out to investigate size dependencies in section 4.

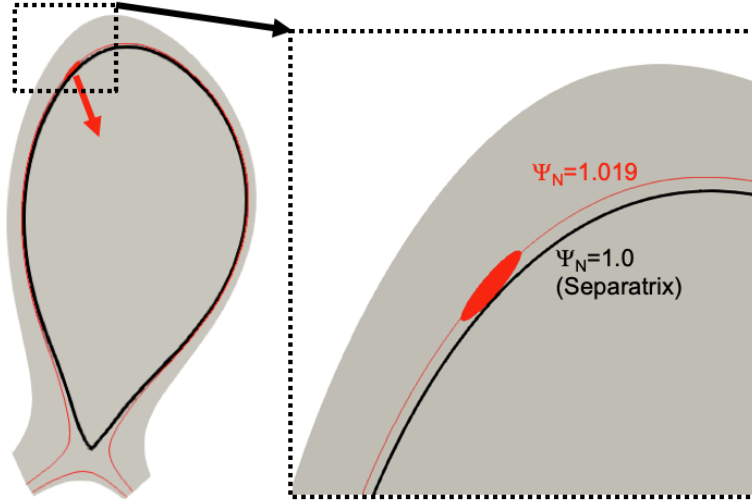


Figure 1: The pellet trajectory is started on the realistic experimental trajectory just outside the separatrix (to save computational time). The red arrow indicates the pellet trajectory into the plasma.

Simulations are carried out with the non-linear MHD code JOREK [18] based on a fully implicit time stepping, and a spatial discretization with 2D Bezier elements in the poloidal plane combined with a toroidal Fourier expansion [34]. The extended physics model including ExB and diamagnetic background flows described in Ref. [21] is used. Mach-1 boundary conditions are applied at the divertor targets to model the plasma sheath at the divertor targets. The injection is performed at different time points during the ELM cycle simulations which are described in Ref. [25]. Details of the ablation and pellet model are described in Refs. [24, 29].

The mechanism of pellet ELM triggering is illustrated based on the simulation with the pellet containing 0.8×10^{20} deuterium atoms injected at 12 ms during the pedestal build-up which is explained in detail later on. Figure 2 shows the high density pellet cloud (pink band). The contour is plotted at $1.3 \times 10^{20} \text{ m}^{-3}$ at the time of the maximum ablation rate $t = 12.274 \text{ ms}$ which is one of the time slice of the inter-ELM, described in Section 3. The pellet ablation is adiabatic and, as it proceeds, the localized high density region created by the ablation of the pellet expands along field lines with the local sound speed. The pellet cloud is heated by the electrons along the magnetic field line with the parallel thermal diffusion which is much faster than the pellet cloud expansion. The resulting local high pressure perturbation is responsible for the ELM onset.

3 Pellet injections at different times during pedestal build-up

In this entire section, we focus only on simulations with a pellet size corresponding to $0.8 \times 10^{20} \text{ D}$ atoms injected at 560 m/s while considering different injection times. Figure 3 shows the time evolution of pressure, temperature and density at the pedestal top during

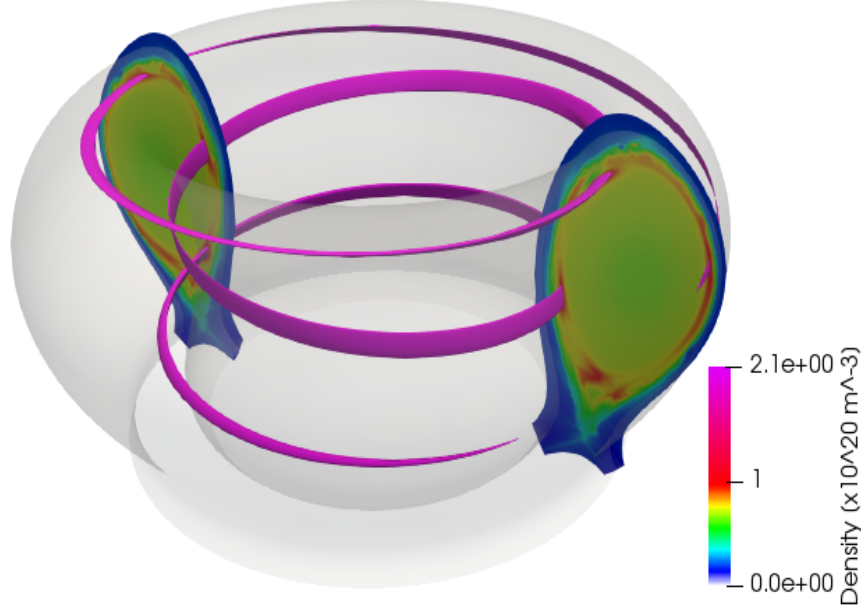


Figure 2: The pellet cloud (pink band) which is defined by $1.3 \times 10^{20} \text{ m}^{-3}$ at the timing of the maximum ablation rate $t = 12.274 \text{ ms}$ ($t_{\text{injection}} = 12 \text{ ms}$).

the inter-ELM period in the JOREK ELM cycle simulation used as basis for the present study. The post-ELM profiles build up until they reach the MHD stability limit and a natural ELM crash eventually occurs at about 16 ms causing a significant loss of particles and thermal energy [25]. Figure 4 shows the profiles of toroidally averaged pedestal pressure and the current density for the time slices 0.5 ms, 2 ms, 4 ms, 6 ms, 8 ms, 10 ms, 12 ms, 14 ms and 15 ms. Table 1 shows the pellet injection timings and corresponding pedestal parameters. Here, the pedestal top is considered at $\Psi_N \sim 0.932$ and the peak of the current density profiles at the outer midplane are given at $\Psi_N \sim 0.973$, where it peaks.

Pellet injections are simulated at different times during build-up which correspond to evolving MHD stability conditions (0.5 ms, 2 ms, 4 ms, 6 ms, 8 ms, 10 ms, 12 ms, 14 ms and 15 ms). Figure 5(a) and (b) show the ablation rates versus time ($t - t_{\text{injection}}$) and versus normalized poloidal magnetic flux, respectively for the different injection times. The ablation process for this pellet size completes within 0.5-0.6 ms depending on the chosen injection time. The pellet is injected with the velocity 560 m/s, and it reaches the separatrix in 0.033 ms which is very fast compared to the time-scale of MHD activities and pellet ablation physics which we are looking at. When the pellet crosses the separatrix, it starts ablating according to the local plasma parameters such as density and temperature. The pellet injection timing gives different pellet ablation rate, in terms of the maximum ablation rate and the pellet penetration depth due to the different plasma parameters at those times. Specifically, pellet ablation for early

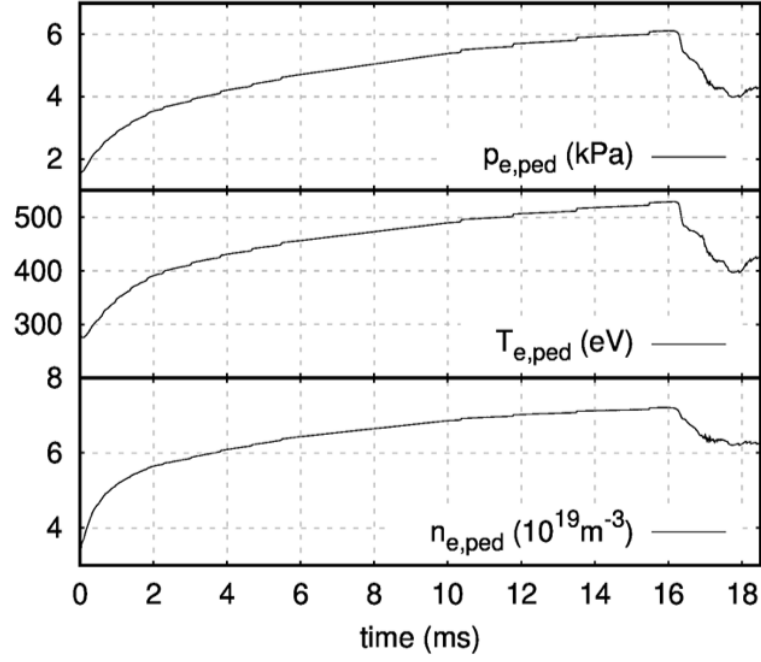


Figure 3: The time evolution of the pressure, the temperature and the density at the pedestal top of the base natural ELM case taken from the series of simulations described in Ref. [25]. Pellet injection simulations are modelled at different times during the build-up phase. Losses from the natural ELM can be seen to start at about 16.1 ms.

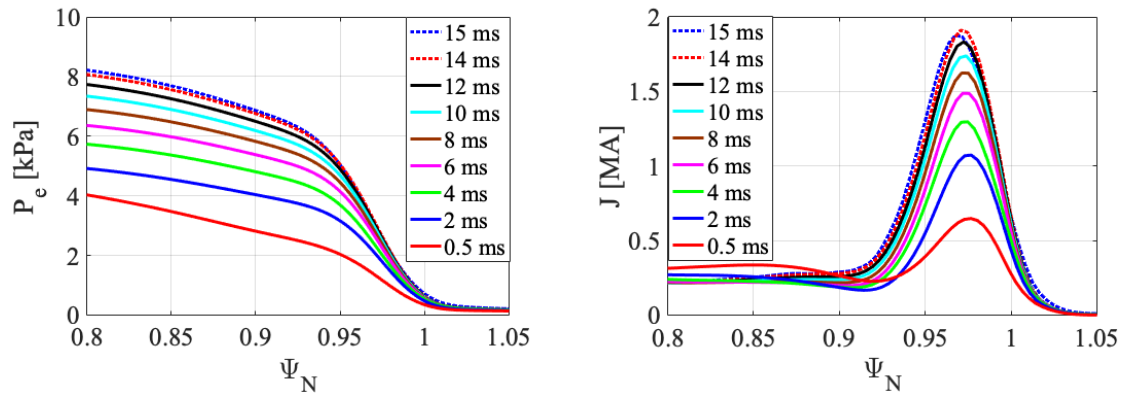


Figure 4: Profiles of toroidal averaged electron pressure (p_e) and current density (J) in the pedestal region for the injection times 0.5, 2, 4, 6, 8, 10, 12, 14 and 15 ms.

Table 1: The pellet injection timings and corresponding pedestal parameters (the electron pressure at the pedestal top $\Psi_N \sim 0.932$ and the current density at $\Psi_N \sim 0.973$).

inj. time	electron pressure p_e	current density J
0.5 ms	2.4 kPa	0.65 MA
2 ms	3.7 kPa	1.07 MA
4 ms	4.3 kPa	1.30 MA
6 ms	4.8 kPa	1.49 MA
8 ms	5.3 kPa	1.63 MA
10 ms	5.6 kPa	1.74 MA
12 ms	5.8 kPa	1.83 MA
14 ms	6.0 kPa	1.91 MA
15 ms	6.1 kPa	1.88 MA

injections in the cycle (0.5 ms, 2 ms, 4 ms, 6 ms and 8 ms) takes longer than for late-injection cases since the temperature is lower. As a consequence, early injection cases show deep pellet penetration into the plasma, reaching $\Psi_N < 0.65$. In case of later injection, the ablation rate starts to drop around $\Psi_N = 0.95$ due to the collapse (relaxation) of the pedestal structure (the ELM crash). Still, the penetration depth in case of late injection remains shallower due to the higher ablation rate in the hotter plasma.

Table 2 summarizes the information of the maximum ablation rate and the full ablation rate for the dependence of pellet injection timings.

Table 2: List of the simulation cases which are performed for this section with information regarding time of the maximum ablation rate and the full ablation.

inj. time	Time at max. abln.	Ψ_N at max. abln.	Time at full abln.	Ψ_N at full abln.
0.5 ms	0.8088 ms	0.80	1.1013 ms	0.5456
2 ms	2.2635 ms	0.842	2.573 ms	0.574
4 ms	4.2635 ms	0.845	4.546 ms	0.6018
6 ms	6.2136 ms	0.8835	6.527 ms	0.6216
8 ms	8.2164 ms	0.8781	8.5068 ms	0.6374
10 ms	10.226 ms	0.872	10.496 ms	0.6493
12 ms	12.274 ms	0.8376	12.4967 ms	0.6513
14 ms	14.268 ms	0.8384	14.488 ms	0.6562
15 ms	15.3045 ms	0.813	15.5035 ms	0.6456

Figure 6 shows the particle and the energy content inside of the separatrix versus time for different pellet injection times. The pellet size is 0.8×10^{20} and the injection velocity is 560 m/s. The time evolution of the particle content clearly indicates that the pellets deliver particles into the plasma. In case of late injections (≥ 12 ms), the increase of the particle content in the separatrix is significantly below the pellet content (0.8×10^{20})

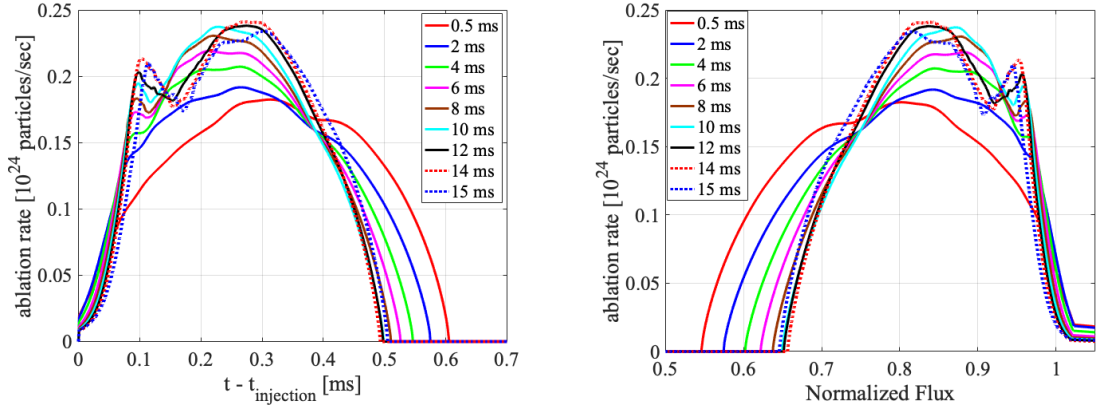


Figure 5: (a) The time evolution of the pellet ablation rate for different pellet injection timings versus $t - t_{\text{injection}}$. The pellet size is 0.8×10^{20} D and the injection velocity is 560 m/s. (b) The pellet ablation rate versus normalized poloidal magnetic flux.

since the pellet-triggered ELM expels particles from the plasma. For the same reason, a strong drop of the plasma thermal energy content is observed when the pellet is injected at 12 ms or later. In order to compare the variation of the particle and the energy content inside the separatrix, the evolutions are normalized with respect to the values at pellet injection as shown in Fig. 7. There is a sharp transition in the thermal energy drop between the pellet injection timings of 10 ms and 12 ms.

Figure 8 shows the relative loss of plasma thermal energy for different pellet injection time. The energy loss is measured as the difference between the maximum value before the crash and the minimum value before the thermal energy starts to increase again and is then normalized by the total plasma thermal energy before the crash to obtain the relative value. Pellet injections at very early timings, 0.5 ms and 2 ms do not show energy losses at all according to this definition (no minimum in the thermal energy content; however, the injection still causes a reduction in comparison to the case without injection as seen in Figure 6). The injection timings of 4 ms, 6 ms, 8 ms, and 10 ms show energy losses of $\leq 1\%$. There is a sharp transition in the thermal energy loss between cases where no ELM is triggered (0.5 - 10 ms) and case (12 ms - 15 ms) where an ELM is triggered. The injection times should not be compared one to one to the experiment, since the pedestal build-up might not be identical. Instead, we analyze the pedestal parameters corresponding to the transition between the no-ELM triggering and ELM triggering regimes in Figure 4.

Figure 9 shows the power load onto the inner and the outer divertor targets which is caused by 0.8×10^{20} D pellet injections. Most of the power goes to the divertor targets. There is a sharp transition in the peak of the integrated power load onto the divertor targets between cases where no ELM is triggered (≤ 10 ms) and cases where ELMs are triggered (≥ 12 ms). The peak of the power load onto the outer divertor target in no

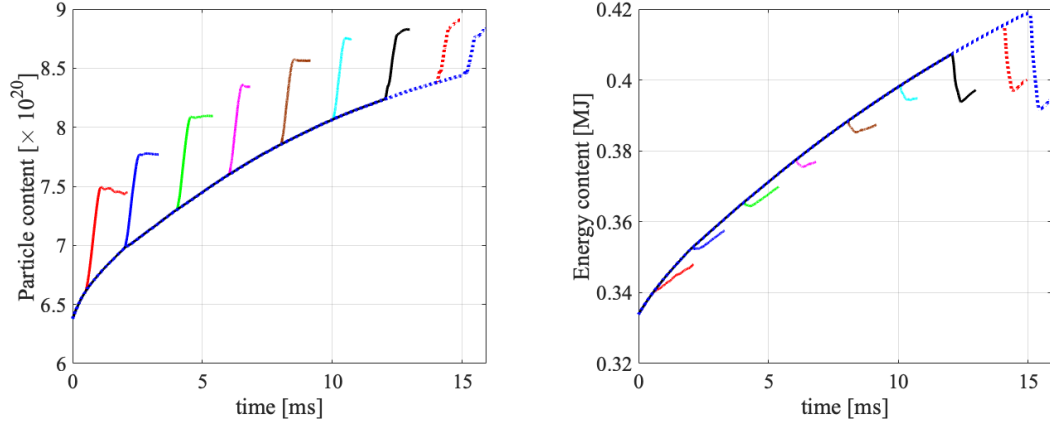


Figure 6: (a) The particle and (b) the energy content inside of the separatrix versus time for different pellet injection timings. The pellet size is $0.8 \times 10^{20}D$ and the injection velocity is 560 m/s.

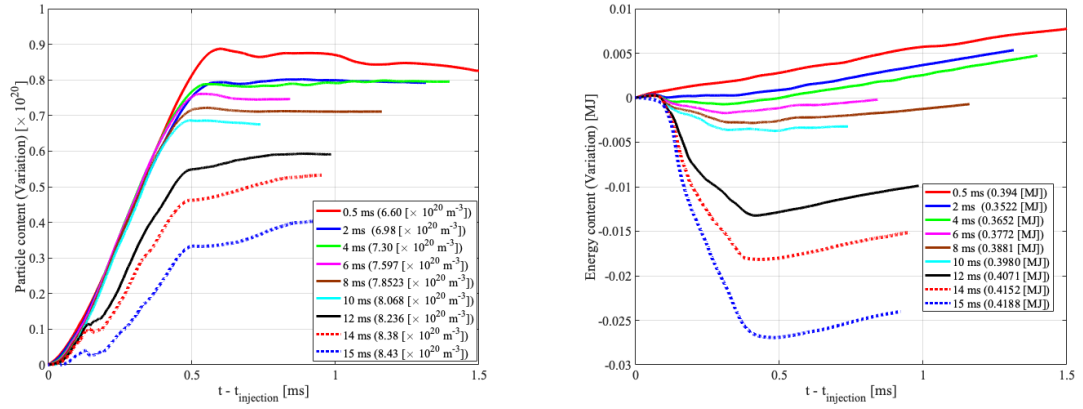


Figure 7: (a) The particle and (b) the energy content inside the separatrix versus time for different pellet injection times. The x-axis is shifted with respect to the injection time. For the y-axis, the difference between the injection case and an equivalent axisymmetric simulation without injection is plotted.

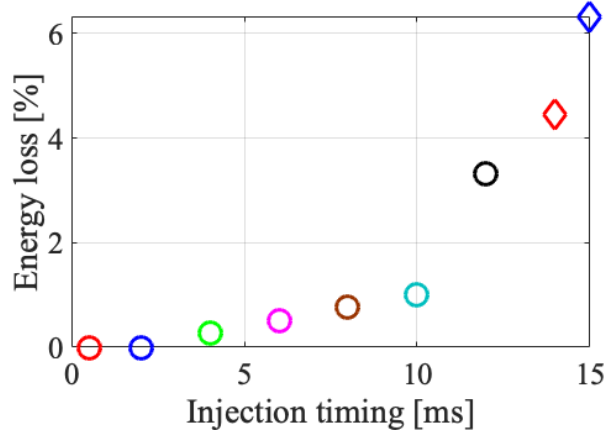


Figure 8: The thermal energy loss in percentage for different pellet injection times. The pellet size is $0.8 \times 10^{20}\text{D}$ and the injection velocity is 560 m/s.

ELM triggered cases (≤ 10 ms) is ≤ 5 MW. The peak of the power load onto the outer divertor target where ELMs are triggered (≥ 12 ms) reaches ≥ 10 MW, especially late injection cases (≥ 14 ms) shows ≥ 20 MW power load onto the outer divertor target. A strong increase of the power load is observed to last roughly 0.4 ms due to the pellet-triggered ELM. The outer divertor target receives about twice as much power as the inner target like pretty universal for the simulations performed in this study. The distribution of the heat between the targets should not be compared directly to the experiment, since the SOL model used in the simulations is very simplified and remains to be enhanced in future studies.

The pellet is injected at the toroidal angle of 0 degree ($\varphi = 0$). The heat flux profile onto the outer divertor target at $\varphi = 0$ versus time is shown in Fig. 10 for the pellet injection times of 8 ms, 10 ms and 12 ms. It is clearly visible that the cases without ELM triggering do not show prominent increases of heat flux onto the divertor. On the other hand, the case of pellet injection at 12 ms shows a strong increase of the heat flux $\sim 20 \text{ MW/m}^2$ at the strike point for 12.1 ms - 12.5 ms.

Figure 11 shows the heat flux profile at the maximum power load onto the outer divertor target (see Fig. 9). The early injection cases (0.5 - 10 ms) which do not trigger an ELM show a peak heat flux of $\leq 10 \text{ MW/m}^2$. The cases which do trigger ELMs ($t_{\text{inj.}} \geq 12$ ms) show a peak heat flux of $\geq 20 \text{ MW/m}^2$. Peak heat fluxes for pellet injection at 14 ms and 15 ms are $\geq 30 \text{ MW/m}^2$. The heat flux profiles of these pellet-triggered ELMs display toroidally asymmetric characteristics which are described in the following paragraph. The wetted area as well as many other non-linear features of the simulated pellet-triggered ELMs in comparison to spontaneous ELMs is described in detail in Ref. [32].

Toroidally asymmetric features of the pellet-triggered ELM and a sub-structure in the heat deposition with several peaks are observed, and are qualitatively similar to previous simulations for JET [29]. The heat flux profile versus the toroidal angle in the

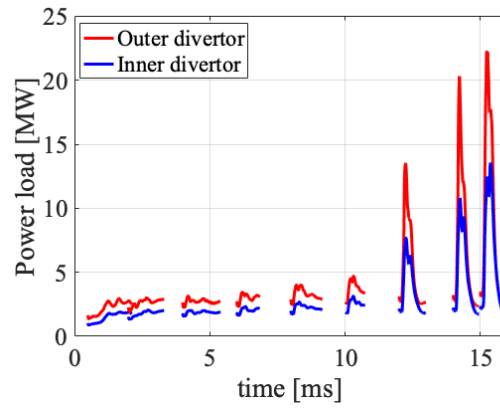


Figure 9: The time evolution of the power load onto the inner and the outer divertor targets which is caused by $0.8 \times 10^{20} D$ pellet injections for the various injection times.

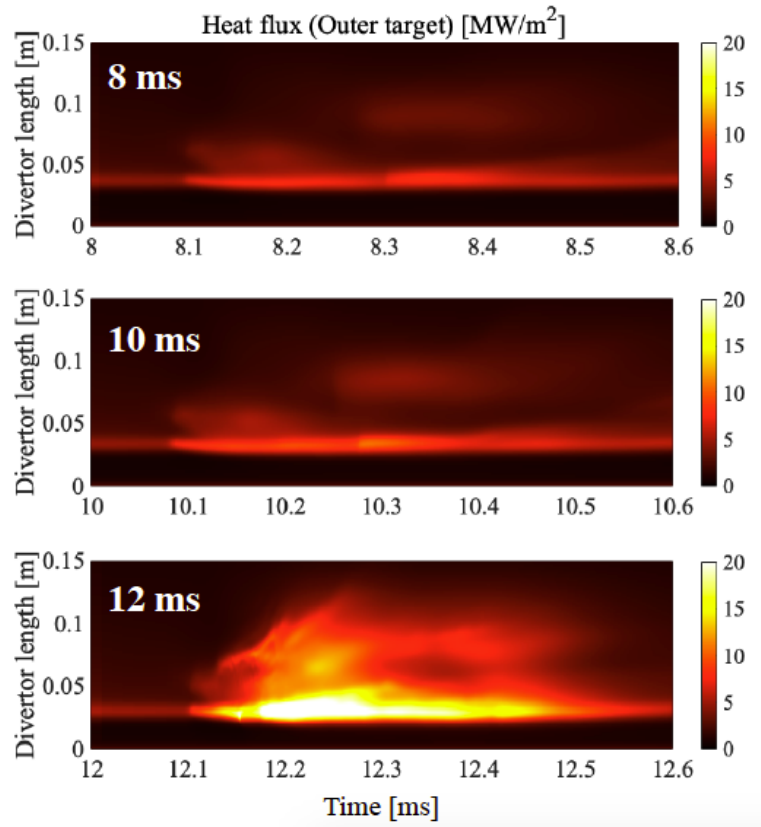


Figure 10: The time evolution of the heat flux onto the outer divertor targets which is caused by $0.8 \times 10^{20} D$ pellet injection with the injection velocity of 560 m/s. Three cases are compared where only the last one corresponds to a pellet-triggered ELM case (12 ms).

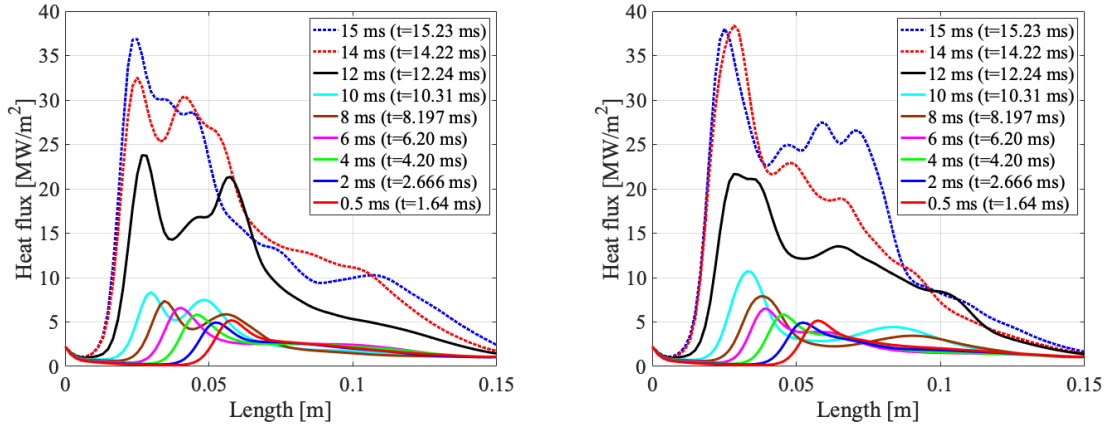


Figure 11: Heat flux profiles of the outer divertor target at maximum power load onto the outer divertor target for the various cases with different injection times (see Fig. 9). The left panel shows the heat flux profiles at a toroidal angle of 180 degrees ($\varphi = 180^\circ$) and the right panel shows the ones at the toroidal angle of 0 degrees ($\varphi = 0^\circ$), i.e., at the toroidal angle of pellet injection.

case with 0.8×10^{20} D pellet injection at $t_{\text{inj.}} = 12$ ms is shown in Fig. 12. The time slice of $t = 12.24$ ms with the maximum power load onto the plasma facing components is plotted. A strongly asymmetric profile of the heat flux profile is observed. The observation of $n = 1$ toroidal structure is universal in all cases of pellet-triggered ELMs in this study.

Figure 13 shows the heat flux profile versus time for the toroidal angle of $\varphi = 180^\circ$ and $\varphi = 0^\circ$ for the pellet injection at 12 ms. Due to the toroidally asymmetric characteristics of the pellet-triggered ELM, the time evolution of the heat flux profile at these angles is different.

In this section, the plasma response to pellet injection at different times during pedestal build-up was analysed. The simulations in this section were all carried out with pellets containing 0.8×10^{20} deuterium atoms and an injection velocity of 560 m/s in order to investigate the change of the MHD stability during the pedestal build-up. Realistic ExB and diamagnetic background flows have been included to account for the stabilizing effects accurately. The simulations clearly show a sharp transition between early injection with moderate losses and divertor heat fluxes (lag-time) and later injections with an explosive onset of MHD instabilities causing strong losses and large divertor heat fluxes. The threshold for pellet ELM triggering is here between a pedestal pressure of $p_{\text{e,ped}} = 5.6$ and 5.8 kPa which corresponds to the injection timings of 10 ms and 12 ms. In Section 4, we investigate the influence of the pellet size onto the observed lag-time.

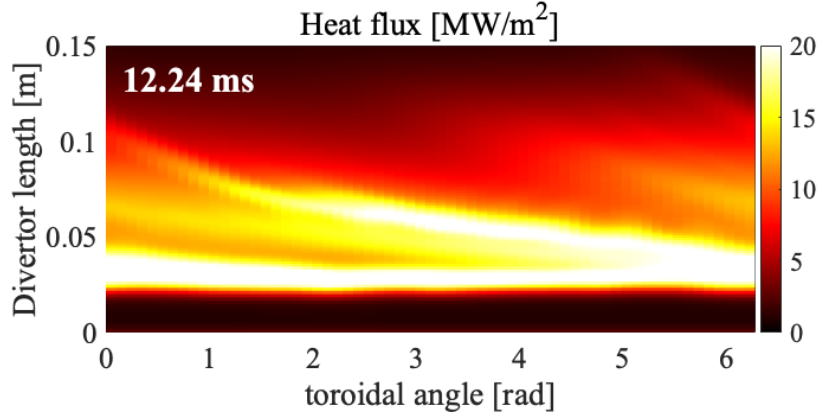


Figure 12: The heat flux profile along the toroidal direction in the case with injection at 12 ms, which triggers an ELM. The outer divertor target is shown at $t = 12.24$ ms (time of maximum heat flux). A strongly asymmetric structure is observed with a clear strike-line splitting.

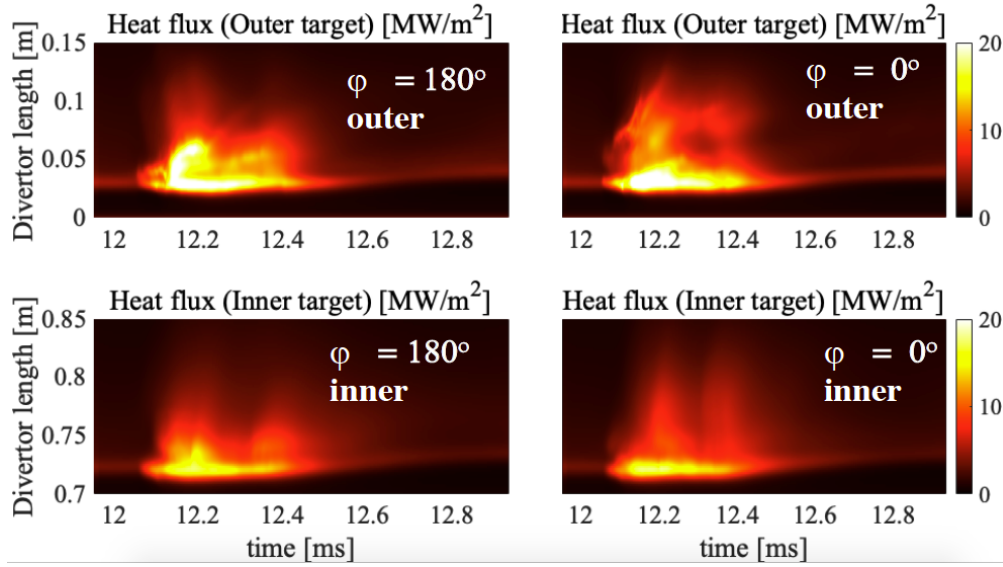


Figure 13: The heat flux profile versus time for the toroidal angle of (left) $\varphi = 180^\circ$ and (right) $\varphi = 0^\circ$ where the $0.8 \times 10^{20} D$ pellet is injected at 12 ms. The outer target is shown at the top, the inner target at the bottom.

4 Pellet size dependency

4.1 Lag-time dependency on the pellet size

While the entire Section 3 dealt with the pellet-triggering for a pellet size of 0.8×10^{20} D atoms, we are now turning to different pellet sizes of 0.4×10^{20} and 1.5×10^{20} D atoms to investigate the dependency of the plasma response on the pellet size. The injection speed remains at 560 m/s for all the cases presented in this section. Note here, that the 0.4×10^{20} D atoms pellet contains less deuterium atoms than the smallest experimentally achievable pellet sizes (even after taking into account losses in the guide tube). Simulations with this pellet size are included here only to have smaller and larger pellet sizes than the base (0.8×10^{20} D atoms) configuration we are studying. Small pellet (0.4×10^{20}) injections are performed at 8 ms, 10 ms, and 12 ms. An ELM crash is not triggered in any of these cases such that we do not present a detailed analysis here.

For the larger pellet size of 1.5×10^{20} D atoms, we analyze the simulation results in the following and investigate the lag-time for pellet ELM triggering. Figure 14 shows the time evolution of the particle and the thermal energy content inside the separatrix for different pellet injection times. The pellets which are injected at 4 ms and 6 ms deliver all particles contained in the pellet into the plasma (1.5×10^{20} particles). The pellets which are injected at 8 ms or later show that the increase of the particle content in the plasma is less than 1.5×10^{20} D due to the pellet-triggered ELM losses. Figure 14(b) shows a clear difference in the drop of energy between 6 ms and 8 ms injection time (also with a much large loss rate at 8 ms), as well demonstrating that the lag-time during which pellet ELM triggering is not possible ends now between 6 and 8 ms instead of 10 and 12 ms for the base pellet size (0.8×10^{20}). The larger pellets allow to excite plasmas in more stable MHD condition (earlier time during build-up).

Figure 15 shows the relative loss of the total plasma thermal energy for different pellet injection timing. There is a transition in the thermal energy loss between cases where no ELM is triggered (4 - 6 ms) and case (8 ms - 14 ms) where an ELM is triggered. From the plot of the energy loss in Fig. 15, the transition between 6 ms and 8 ms is less clear than the study of 0.8×10^{20} D pellets (which is shown in Fig. 8). With the pellet size of 1.5×10^{20} D, the pellet injections at earlier stage, less than 6 ms induce thermal energy loss although the loss is much smaller than the ELM loss. Therefore the transition of the thermal energy content between no ELM cases (4 - 6 ms) and ELM triggering cases (8 ms - 14 ms) is less clear. The transition becomes more visible in the plot of the power load onto the divertor target. Figure 16 shows the power load onto the inner and the outer divertor targets which is caused by 1.5×10^{20} D pellet injections with 560 m/s. There is a clear transition in the heat loads between the regime where no ELM is triggered (simulations with $t_{\text{inj.}} \leq 6$ ms) and the regime where the pellet injection causes an ELM crash ($t_{\text{inj.}} \geq 8$ ms). The duration of the peak of the power load of the pellet-triggered ELMs is roughly 0.4 ms and therefore very similar to the base pellet (0.8×10^{20} D) ELM triggering.

The heat flux profile along the toroidal angle in the case of the injection at 10 ms triggering an ELM is shown in Fig. 17. The time slice of $t = 10.22$ ms which is at the

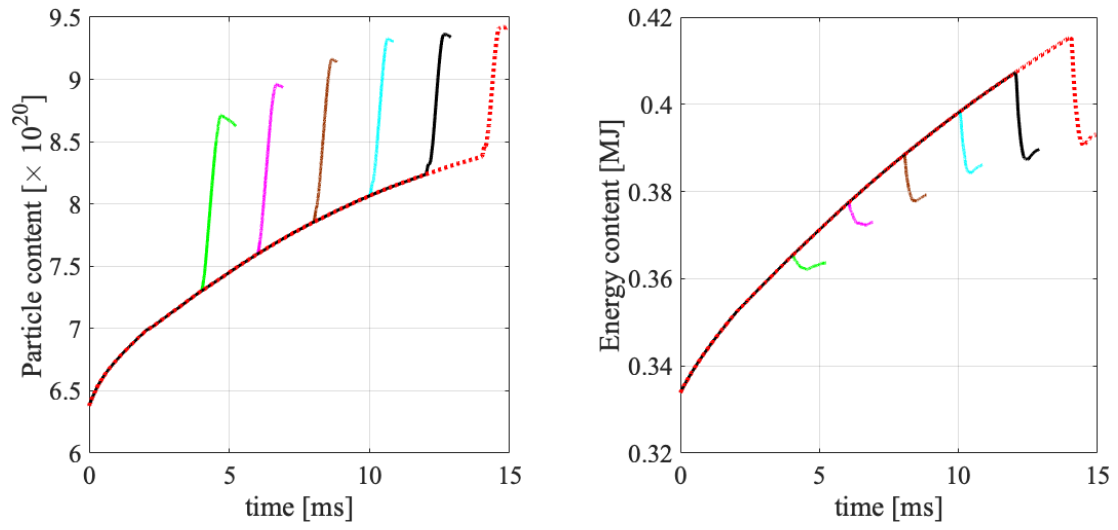


Figure 14: The time evolution of (left) the particle and (right) the energy content inside the separatrix for different injection times of the large pellet ($1.5 \times 10^{20} D$) with 560 m/s.

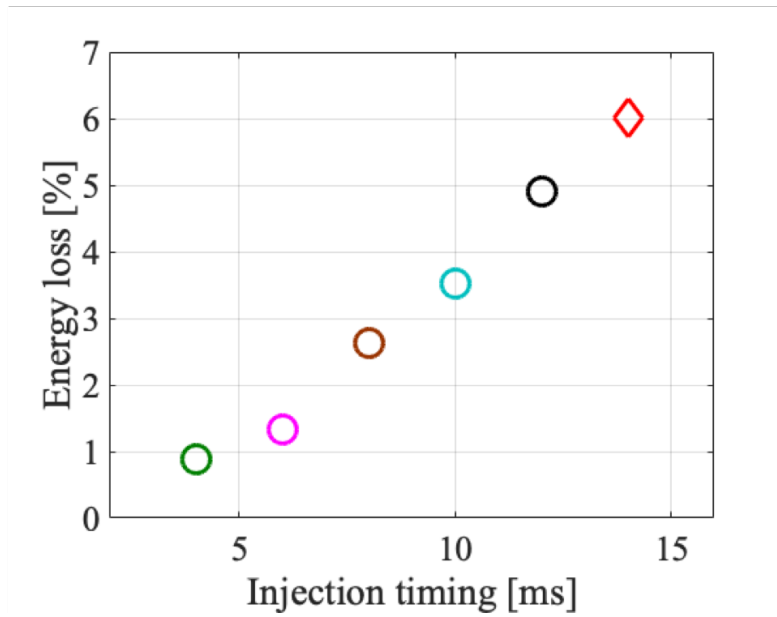


Figure 15: The relative loss of thermal energy for different injection timing with $1.5 \times 10^{20} D$ pellets at an injection velocity of 560 m/s.

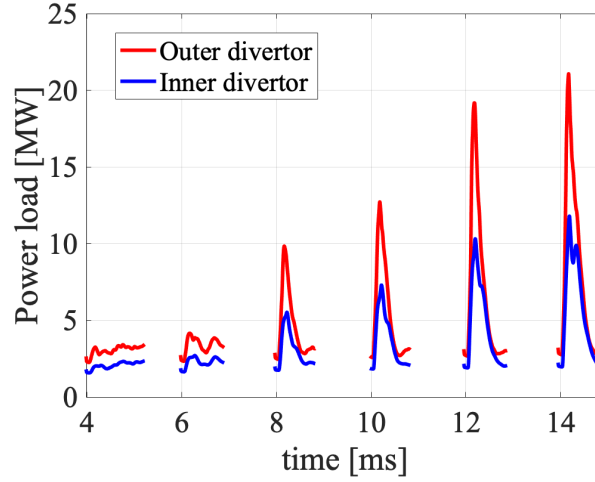


Figure 16: The time evolution of the power load onto the inner and the outer divertor targets which is caused by $1.5 \times 10^{20} D$ pellet injections with 560 m/s of pellet injection velocity.

maximum power load onto the outer divertor is plotted. The heat flux profile along the toroidal angle is observed to be toroidally asymmetric like those for ELMs induced by the base pellets ($0.8 \times 10^{20} D$). It is important to emphasize that the structure (footprint) of the heat flux profile along the toroidal angle is largely independent from the pellet size which triggers the ELM crash. The footprint of the heat flux onto the divertor target is characterized by the magnetic field configuration, which is determined by the ELM crash itself. It, however, deviates from a typical spontaneous ELM crash since the seed perturbation is highly localized in the triggered ELM case as discussed in detail in Ref. [32].

Figure 18 shows the heat flux profile versus time for the toroidal angle of $\varphi = 180^\circ$ and $\varphi = 0^\circ$ where the large pellet ($1.5 \times 10^{20} D$) is injected with 560 m/s. The toroidal asymmetry of the incident heat flux profile for large pellets ($1.5 \times 10^{20} D$) is more pronounced than for the base pellet ($0.8 \times 10^{20} D$) injection (see Fig. 13). In the heat flux profile at $\varphi = 0^\circ$, the secondary peak appears at the divertor length of 6 cm - 8 cm which is same observation in small pellet injection in Fig. 13. The position of the secondary peak of the heat flux onto the outer divertor target is independent from the pellet size. The position of the secondary peak is also dependent on the magnetic configuration of the plasma, especially q95 [31].

4.2 Summary of pellet size dependence

The pellet size dependence on the pellet-triggered ELM is studied keeping the same injection speed, 560 m/s. Figure 19 shows the pellet ablation rate versus time and versus normalized flux for three pellet sizes, $1.5 \times 10^{20} D$, $0.8 \times 10^{20} D$ and $0.4 \times 10^{20} D$, injected at 12 ms. The pellet ablation duration increases with pellet size from 350 μs for the smallest

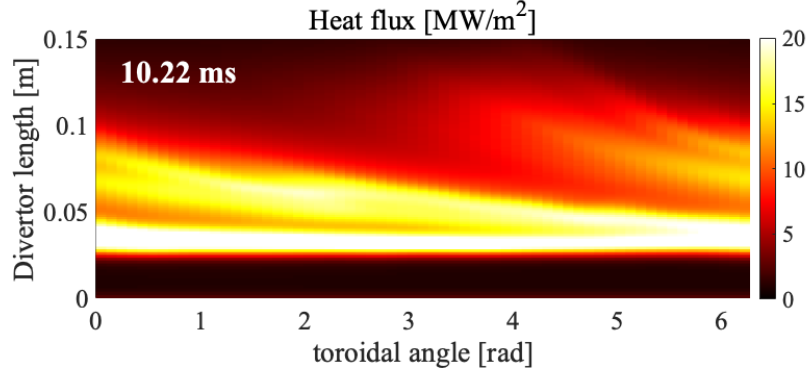


Figure 17: The heat flux distribution on the outer target in the case of injection at 10 ms which triggers an ELM. The plot corresponds to the time of maximum power load onto the outer divertor target, 10.22 ms.

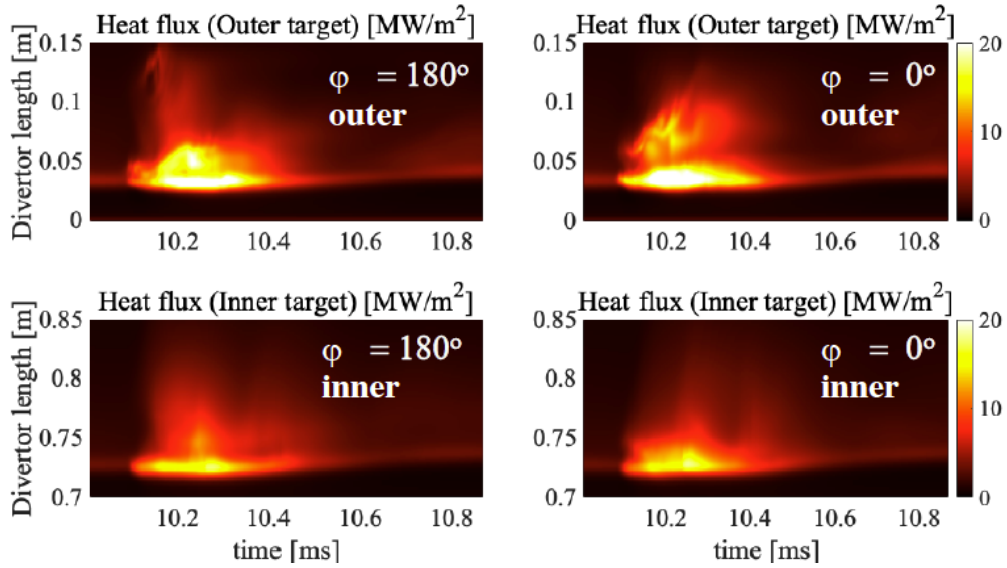


Figure 18: The heat flux profile versus time after 1.5×10^{20} D pellet injected at 10 ms is plotted for the toroidal angle of (left) $\varphi = 180^\circ$ and (right) $\varphi = 0^\circ$. The latter corresponds to the toroidal location of pellet injection. The outer target is shown at the top, the inner target at the bottom.

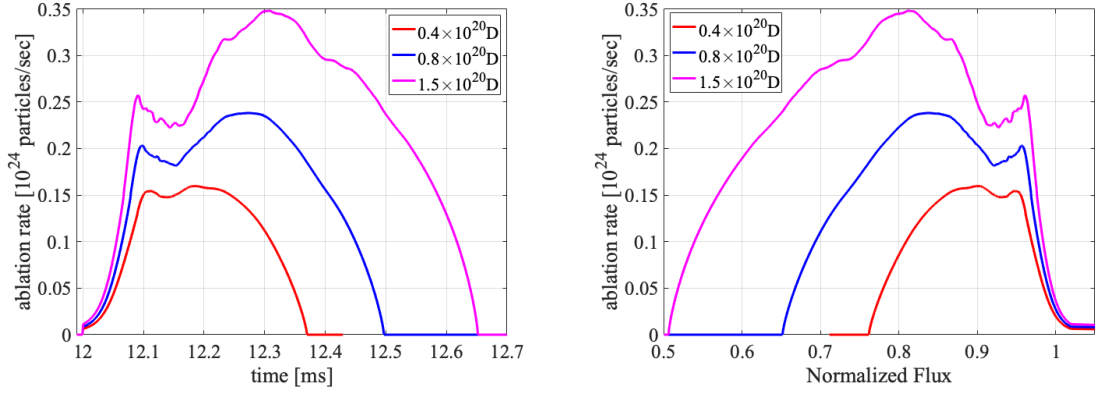


Figure 19: The time evolution of (left) the particle and (right) the energy content inside the separatrix for different injection times and different pellet sizes (keeping a fixed injection velocity of 560 m/s).

pellet to $650 \mu\text{s}$ for the largest pellet. All pellet sizes which have been studied in the work penetrate beyond the pedestal top ($\Psi_N \sim 0.93$). The large pellets can reach the core plasma, $\Psi_N \sim 0.5$. Note, the pellet penetration depth is not possible to be estimated by a simple function of pellet sizes. Because the penetration depth depends on the local temperature and density at the pellet location, and the local temperature and the local density evolve in time not only due to adiabatic ablation, but in particular due to MHD induced transport. Depending on the excited MHD activity, e.g. a pellet-triggered ELM, the local temperature abruptly changes. Therefore, the pellet penetration depth in realistic scenarios can only be obtained from non-linear MHD simulations such as JOREK.

Figure 20 shows the time evolution of the particle and the thermal energy content inside the separatrix for three pellet sizes, $1.5 \times 10^{20} D$, $0.8 \times 10^{20} D$ and $0.4 \times 10^{20} D$ which are injected at 8 ms. The small pellet, $0.4 \times 10^{20} D$, delivers almost all the pellet particles into the plasma while the large pellet, $1.5 \times 10^{20} D$, delivers only 85% of the particles into the plasma because of the pellet-triggered ELM losses. The large pellet $1.5 \times 10^{20} D$ injection also features a prominent drop of the energy content which means the ELM triggering is achieved.

Table 3 summarizes the relative energy loss for different pellet sizes and different injection times. Figure 21 shows the relative thermal energy loss for the different pellet injection times and different pellet sizes, i.e., the data from Table 3. The following cases show less than 1.5 % of the energy loss, i.e. no pellet ELM triggering is achieved;

1. The large pellets ($1.5 \times 10^{20} D$) injected at 4 ms and 6 ms
2. The base pellets ($0.8 \times 10^{20} D$) injected at 10 ms or earlier,
3. The small pellets ($0.4 \times 10^{20} D$) injected at all the probed injection times (very late injections were not simulated since the pellet size is anyway not experimentally

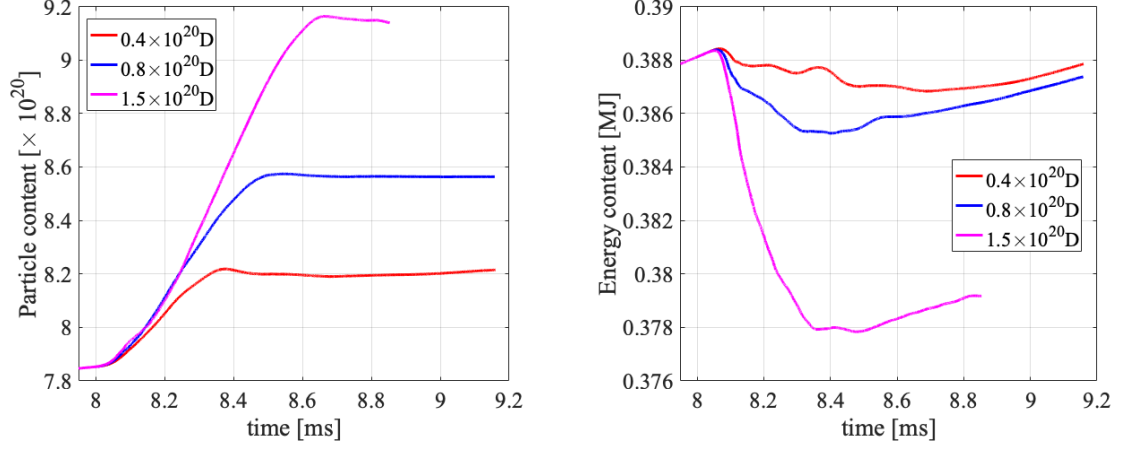


Figure 20: The time evolution of the particle and the thermal energy content inside the separatrix for three pellet sizes, $1.5 \times 10^{20}D$, $0.8 \times 10^{20}D$ and $0.4 \times 10^{20}D$ which are injected at 8 ms (all with 560 m/s).

pellet size	4 ms	6 ms	8 ms	10 ms	12 ms	14 ms	15 ms
$0.4 \times 10^{20}D$	—	—	0.33%	0.38%	0.82%	—	—
$0.8 \times 10^{20}D$	0.27%	0.5%	0.77%	1.0%	3.32%	4.45%	6.33%
$1.5 \times 10^{20}D$	0.88%	1.32%	2.63%	3.52%	4.91%	6.02%	—

Table 3: The energy loss of all injections with 560 m/s performed in this work are listed. The ELM triggering cases are highlighted with blue font. Cases marked with “—” were not simulated.

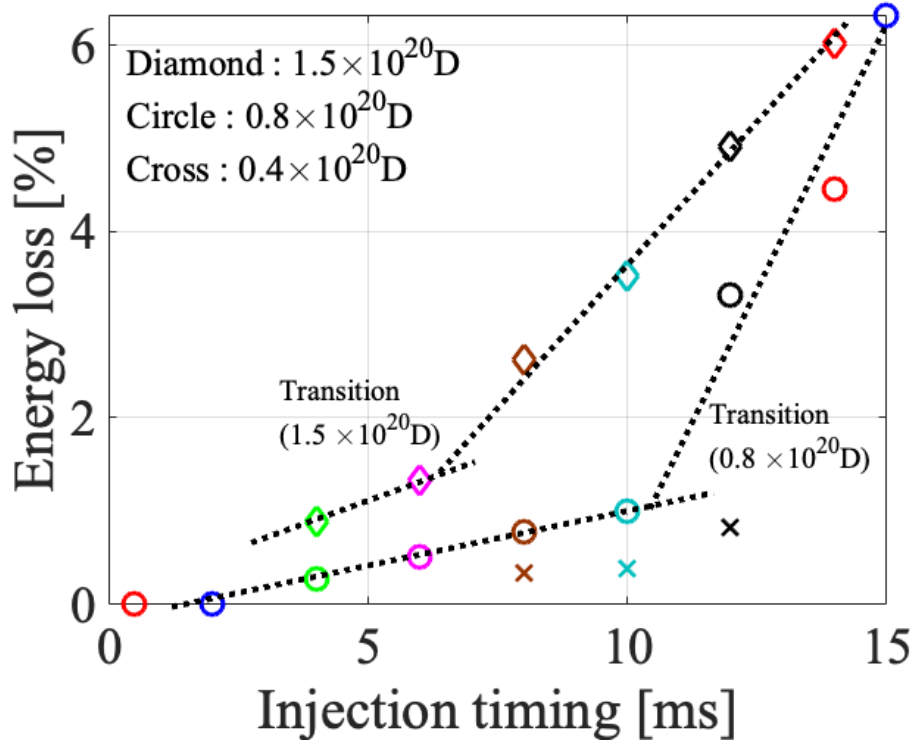


Figure 21: The relative thermal energy loss is shown for different pellet injection timings and pellet sizes. A clear transition between no-ELM and ELM triggering regimes are seen for the medium and large pellet sizes (dotted lines are shown to guide the eye).

relevant for ASDEX Upgrade).

The following cases show more than 2 % energy loss, i.e. pellet ELM triggering is achieved;

1. The large pellets ($1.5 \times 10^{20}D$) injected at later than 8 ms,
2. The base pellets ($0.8 \times 10^{20}D$) injected at after 12 ms.

Figure 22 shows the time evolution of the spatially integrated power load onto the divertor target versus time. All three pellet sizes $1.5 \times 10^{20}D$, $0.8 \times 10^{20}D$ and $0.4 \times 10^{20}D$ and injection timings of 8 ms, 10 ms and 12 ms are included. From the pellets injected at 8 ms and 10 ms, only the large pellet, triggers an ELM and the peak of the integrated power load onto the outer divertor target reaches ~ 10 MW and ~ 13 MW, respectively. Pellets of $0.4 \times 10^{20}D$ and $0.8 \times 10^{20}D$ do not trigger an ELM, with the integrated power load on to the outer target is ≤ 5 MW. For pellet injection at 12 ms, the large pellet $1.5 \times 10^{20}D$ and the middle size $0.8 \times 10^{20}D$ trigger an ELM and the peak of the integrated power load onto the outer divertor target reaches ~ 18 MW and ~ 13 MW, respectively. At this injection time, the smallest pellet does not trigger an ELM crash. All pellet-triggered cases show an ELM duration around ~ 0.4 ms, independent from the pellet size or pellet injection timings. The ELM duration is estimated here from the time of strongly increased divertor heat fluxes. Other definitions like used in the experiment (e.g., D_α signal) might change the time scale slightly, but are not accessible in our simulations directly.

The scan of the pellet parameters shows that the pellet size and the pellet injection timing are essential parameters to determine whether pellet ELM triggering is possible. The toroidal localization of the heat flux and the radial localization of the secondary peak of the heat flux caused by pellet-triggered ELM are independent from the pellet size and pellet injection timing.

5 Characteristics of no-ELM and ELM-triggering response by pellet injection

This section analyzes the non-linear dynamics of no-ELM and ELM-triggering responses in direct comparison based on the simulations from the previous Section. This aims to highlight why one of two regimes is entered and how they differ from each other.

Figure 23 shows the time evolution of the magnetic energies corresponding to toroidal mode numbers $n = 2, 3, \dots, 12$, $\Sigma_{k=2}^{k=12} E_{k,\text{mag}} \equiv \Sigma_k E_{\text{mag}}$. The $0.8 \times 10^{20}D$ pellet injection shows a clear transition in the qualitative behaviour between the injection times 10 ms and 12 ms. This transition takes place once the injected pellets manage to trigger ELMs, i.e. $t_{\text{inj.}} \geq 12$ ms. The $1.5 \times 10^{20}D$ pellet injection shows a similar transition in the integrated magnetic energy between the injection timings of 6 ms and 8 ms reflecting the ELM triggering from 8 ms onward. Table 4 summarizes the pellet-triggered ELM cases; pellet size, time of the peak of $\Sigma_k E_{\text{mag}}$, pellet location at the peak of $\Sigma_k E_{\text{mag}}$, and the number of pellet particle deposited at the time of the peak of $\Sigma_k E_{\text{mag}}$. The $0.8 \times 10^{20}D$

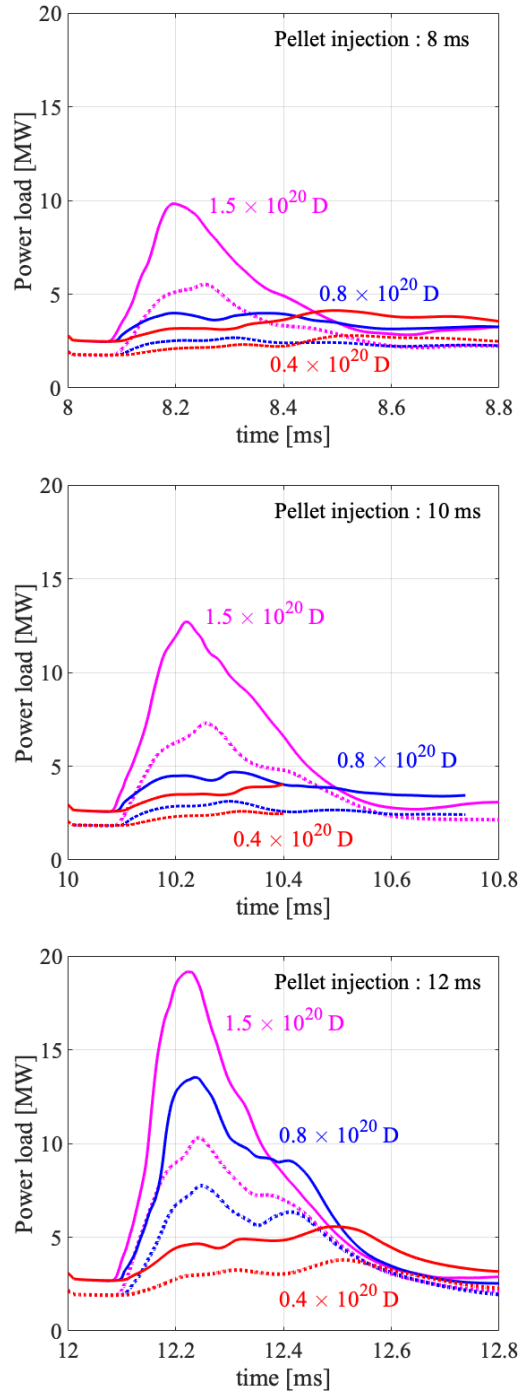


Figure 22: The power load onto the divertor target. The injection of three pellet sizes $1.5 \times 10^{20} D$, $0.8 \times 10^{20} D$ and $0.4 \times 10^{20} D$ for injection times of 8 ms, 10 ms and 12 ms (keeping a fixed injection velocity of 560 m/s). The solid and the dashed lines are outer and inner divertor target, respectively.

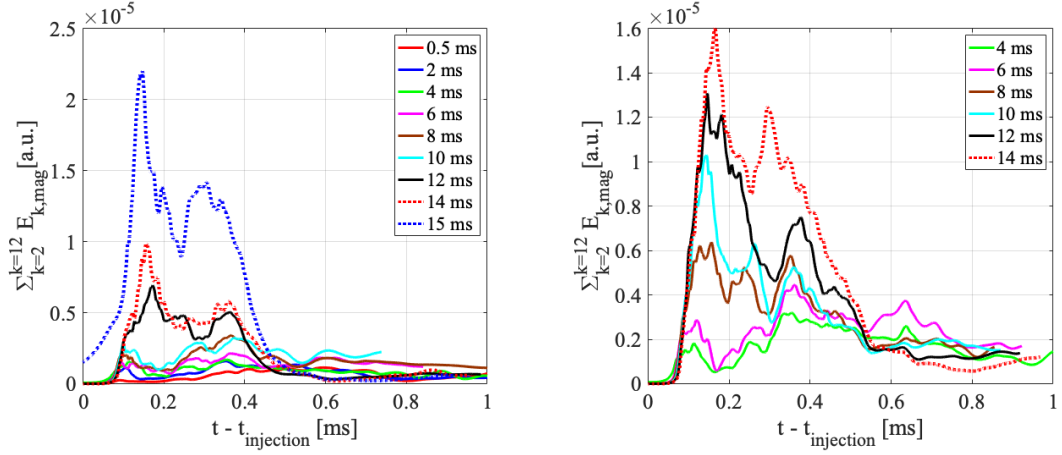


Figure 23: The time evolution of the perturbed magnetic energies in the toroidal mode numbers $n = 2, 3, \dots, 12$ is plotted for different times of pellet injection. The x-axis is shifted with respect to the injection time. The left panel contains the simulations for a pellet size of 0.8×10^{20} atoms. The right panel corresponds to a pellet size of 1.5×10^{20} atoms injected in the pellet.

pellet cases show that for later pellet injection times, the ELM is triggered already at a time when a smaller number of particles has been ablated from the pellet. This is related to the pedestal pressure being closer to marginal stability already, requiring only a smaller 3D pressure perturbation for the ELM triggering. For the large, 1.5×10^{20} D pellet cases, this dependency is less visible.

pellet size	inj. time	peak time	Pellet location	particle deposition
0.8×10^{20} D	12 ms	12.173 ms	0.9081	0.22×10^{20}
0.8×10^{20} D	14 ms	14.152 ms	0.9175	0.1910×10^{20}
0.8×10^{20} D	15 ms	15.1465 ms	0.9223	0.157×10^{20}
1.5×10^{20} D	8 ms	8.154 ms	0.9207	0.2439×10^{20}
1.5×10^{20} D	10 ms	10.143 ms	0.9273	0.217×10^{20}
1.5×10^{20} D	12 ms	12.146 ms	0.9251	0.2189×10^{20}
1.5×10^{20} D	14 ms	14.1608 ms	0.9118	0.2654×10^{20}

Table 4: The summary of pellet size, time of the peak of $\Sigma_{k=2}^{k=12} E_{k,\text{mag}}$, pellet location at the peak of $\Sigma_{k=2}^{k=12} E_{k,\text{mag}}$, and pellet particle deposition in the plasma up to the time of maximum $\Sigma_{k=2}^{k=12} E_{k,\text{mag}}$.

The pellet-induced pressure perturbation of 15 kPa is shown in Fig. 24 as a purple band together with a color contour of the current density on the separatrix at the time of $\max(\Sigma_k E_{\text{mag}})$. The case with the 0.8×10^{20} D atom pellet injected at 10 ms (Fig. 24, left), which does not trigger an ELM, exceeds a pressure perturbation of 15 kPa only in a narrow region around the pellet location. On the other hand, injecting the same pellet

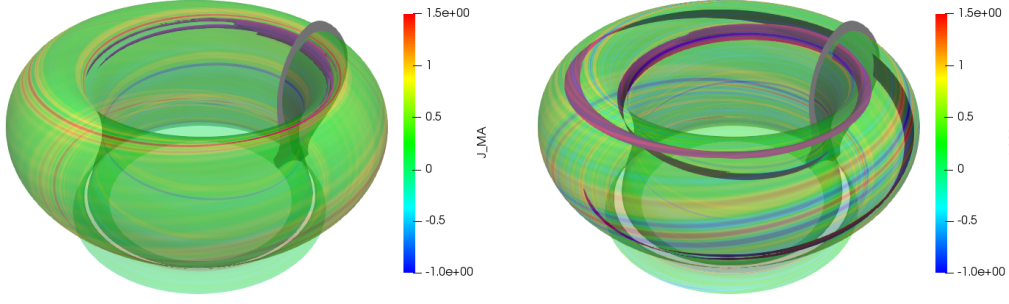


Figure 24: The pellet-induced 3D pressure perturbation of 15 kPa is shown as purple band at the time of the maximum magnetic energy perturbation, $t = 10.097$ ms ($t_{\text{injection}} = 10$ ms) and $t = 12.173$ ms ($t_{\text{injection}} = 12$ ms). Left panel is the pellet injection at 10 ms which does not trigger an ELM, and right panel is injection at 12 ms which triggers an ELM. The pseudocolor plot shows the current density on the separatrix.

size at 12 ms (Fig. 24, right) does trigger an ELM, and leads to a pressure perturbation of ≥ 15 kPa in a for more extended region expanded along the magnetic field lines. For this case, a filamentary ballooning structure in the current density is observed on the separatrix. The key parameter of pellet ELM triggering is this three-dimensional localized pressure perturbation.

It is important to emphasize that there is a delay between the ELM onset, the time of $\max(\Sigma_k E_{\text{mag}})$ and the time slice of the maximum power load onto the outer target ($P_{\text{div,out}}$). Figure 25(a) shows the time evolution of $P_{\text{div,in/out}}$ and of the ablation rate. Figure 25(b) shows the magnetic/kinetic energies of high toroidal modes, $n = 6 - 12$. There is a delay of ~ 0.075 ms between the ELM onset and time at $\max(\Sigma_k E_{\text{mag}})$. There is a delay of ~ 0.142 ms between the ELM onset and the peak of $P_{\text{div,out}}$. The delay in these events is not unexpected as it comes from the distance between separatrix and the divertor target along the magnetic field lines. The heat released from the plasma by the pellet-triggered ELM reaches the divertor target with the time scale of parallel heat diffusion along the stochastic field lines.

Figure 26 shows the toroidal spectrum of the kinetic and magnetic energies which are time-averaged over the pellet ablation process for the base pellet size (see Table 2 for detail information). In case of ELM triggering (12 ms to 15 ms), the non-linear spectrum is significantly broader than in cases without an ELM being triggered. The analysis of the toroidal spectrum is robust. The averaging time-windows over the ELM event which is defined by the excitation of high- n modes shows same conclusion.

Figure 27 shows the Poincaré plots for the pellet locations at $\Psi_{N,p} = 0.94$ and $\Psi_{N,p} = 0.91$, for the injection times of $t_{\text{inj.}} = 8$ ms, 10 ms, and 12 ms. Since the injection velocity and pellet trajectory is the same for all the cases considered here, the pellet position is only dependent on $t - t_{\text{inj.}}$. For each of the investigated pellet positions of $\Psi_{N,p} = 0.94$ and 0.91, the times are $t - t_{\text{inj.}} = 0.12$ and 0.17 ms, respectively. As the pellet enters the

plasma, the confining magnetic field starts to become perturbed and reconnection takes place. Therefore, a stochastic region is formed at the edge of the plasma due to the pellet-induced perturbation. On top of the pellet-induced perturbation, the response of the plasma is present. In fact, there is a visible difference in the response of the confining magnetic field between the cases where no ELM is triggered and the case where the pellet-triggered ELM is present. While the stochastic region reaches only slightly further inwards for the ELM-triggering case, a significantly lower connection length to the divertor targets becomes visible. This can be seen from the far lower density of crossing points in the stochastic region for the late time point (pellet of $\Psi_{N,p} = 0.91$) for the $t_{inj.} = 12$ ms case.

6 Plasma response dependence on pellet injection velocity

While our study has so far investigated different injection times in the ELM cycle and different pellet sizes, we have kept the injection velocity fixed at 560 m/s to avoid changing several parameters at the same time. In this section, we turn now to the influence of the injection velocity. For this purpose, we take the largest pellet size of $1.5 \times 10^{20} D$ atoms, focus on an injection at 8 ms and reduce the injection velocity from our reference value of 560 m/s to 300 m/s and to 240 m/s which are in the achievable range of the experiment [6]. We are well aware, that pellet size and injection velocity cannot be changed fully independently in the experiment and we will discuss this aspect in the conclusions.

Figure 28 shows the pellet ablation rate versus time, and the ablation rate profile versus normalized flux. The reference pellet ($v_p = 560$ m/s) reaches the high-temperature region quickly, therefore the amplitude of the ablation rate is larger than for the cases with slower pellet injection. As the pellet ablates quicker than the slow pellet injection, the duration of the ablation time is shorter, but the faster pellet penetrates deeper. The cases of slower pellet injection stay in the pedestal, i.e. lower temperature region for a longer time. Therefore the pellet ablation rate is lower than the fast injection cases and penetration is not as deep.

Figure 29 shows the time evolution of the particle and the energy content. After reaching the peak of the particle content, the slow injection speeds, 300 m/s and 240 m/s show a drop of the particle content in the plasma. The plot of the energy content shows that the fast pellet injection (560 m/s) induces a large energy drop in a short time, ~ 0.3 ms. On the other hand, the slower pellet injections, 300 m/s and 240 m/s, show comparatively smaller drops of the energy content, i.e., the pellet-triggered ELM energy losses are increasing (in this case) with the injection velocity. The slower pellet injections reach the maximum pellet ablation rate at $\Psi_N = 0.9$ which is close to the pedestal region compared to the reference case (at $\Psi_N = 0.83$), as shown in Fig. 28. The region over which the pellet particles are deposited and the duration of the pellet ablation cause observable differences in terms of the duration of the energy and the particle losses caused by the pellet-triggered ELM.

Figure 30 shows the power load onto the inner and the outer divertor targets which

is caused by $1.5 \times 10^{20} D$ pellets injected at 8 ms, for 560 m/s (reference case), 300 m/s and 240 m/s. The peak of the power load onto the divertor targets is increasing with the pellet injection velocity. The ELM duration is about 0.4 ms independently of the pellet injection velocity.

The pellet injection velocity dependence has additionally been studied with the plasma which is very close to produce the natural ELM. The pellet of $0.8 \times 10^{20} D$ size is injected at 14 ms with two injection velocities: 560 m/s (reference case) and 800 m/s. Figure 31 shows the time evolution of the pellet ablation rate and the pellet ablation rate versus normalized flux for the reference pellet and for the pellet with $v_p = 800$ m/s. The fast pellet reaches the high-temperature region quickly, therefore the pellet ablation rate increases relative to the reference case. As the pellet ablation rate is high, the fast pellet reaches the full ablation quicker than 560 m/s injection case. The fast pellet injection penetrates deeper into the plasma, $\Psi_N \sim 0.55$, while the reference case reaches $\Psi_N \sim 0.65$.

Figure 32 shows the time evolution of the energy content inside the separatrix and the power load onto the divertor targets. The reference case induces a sharper drop of the energy content compared to the faster pellet injection. As consequence, the power load onto the divertor target for the pellet injection with 560 m/s leads to a larger peak power load with respect to the faster pellet injection. The amount of the energy lost after the pellet injections with 560 m/s and 800 m/s is similar, 20.4 kJ and 18.2 kJ, respectively. This observation is in some contrast to the v_p scan with pellets of $1.5 \times 10^{20} D$ atoms injected at 8 ms, where injection at the reference velocity lead to larger losses than at slower v_p .

For the $0.8 \times 10^{20} D$ atoms pellet, injection with $v_p = 560$ and with 800 m/s cause similar ELM induced thermal energy losses. However, while the reference case causes a very fast crash within approximately 250 μ s, the drop of the thermal energy is slower for the case with $v_p = 800$ m/s and it is divided into two separate energy drops. This appears to be linked to the lower material ablation in the pedestal region for the fast injection case. Figure 33 shows the time evolution of $\Sigma_{k=2}^{k=12} E_{k,\text{mag}} \equiv \Sigma_k E_{\text{mag}}$ for the reference case and for the $v_p = 800$ m/s case. The reference case shows the peak of $\Sigma_k E_{\text{mag}}$ at 14.15 ms which is much earlier than the time of full ablation, 14.488 ms. The pellet excites the ELM during the pellet ablation process. On the another hand, the pellet injection of 800 m/s case shows the peak of $\Sigma_k E_{\text{mag}}$ at 14.42 which is after the time of full ablation, 14.40 ms.

Figure 34 shows the Poincaré plots for the pellet locations at $\Psi_{N,p} = 0.94$ and $\Psi_{N,p} = 0.91$, for the injection velocities of 560 m/s and 800 m/s. The pellet injection velocities give slightly different structures of stochastic layer although the width of the layer is comparable when the pellet location is the same. Comparing the Poincaré plots with two different injection velocities shows that the case with $v_p = 560$ m/s has a stochastic region with a far lower connection length. As a result, field lines from this region hit the divertor targets after a lower number of toroidal turns reflected in a lower density of points in the plot. This partly explains the stronger losses observed by the pellet injection at reference velocity.

Besides the different dynamics of the ELM crash, the fast injection also excites core

modes as seen in the Poincaré plots of Figure 35. Figure 36 shows the Poincaré plot in the relaxation state after the ELM crash for the two injection velocities. The times of 14.95 ms ($v_p = 560$ m/s) and 15.1476 ms (800 m/s) which are taken 0.5 ms after the minimum of the thermal energy content are chosen. In the fast pellet injection case (800 m/s), the width of the 2/1 magnetic island is about 3 cm and the width of the 3/1 magnetic island is about 3.5 cm indicating that both might become NTMs in this scenario. In the 560 m/s injection case, the island widths are in the range of 1 cm only and therefore possibly too small for becoming NTMs. The further evolution of these core modes is beyond the scope of this work.

7 Conclusions and Outlook

Non-linear MHD simulations of ELM triggering by pellet injection was studied based on an ASDEX Upgrade H-mode plasma with JOREK including realistic ExB and diamagnetic background flows as well as time-evolving bootstrap current. The pellets are injected at different times in the inter-ELM phase with the pedestal build-up modelled via prescribed ad-hoc diffusion profiles. This simplified approach allows to recover the experimentally observed lag-time for the first time in simulations and to investigate the plasma dynamics resulting from pellet injections at different phases of the build-up. The simulations with 0.8×10^{20} deuterium atoms contained in the pellet (corresponding to an approximately two times larger pellet size in the experiment before the losses occurring in the guide tube), show a sharp transition of the energy losses between early ($t_{inj.} \leq 10$ ms) and later injection times ($t_{inj.} \geq 12$ ms), which correspond to different stages of pedestal build-up. To make the transition comparable to the experiment, the transition is characterized in pedestal parameters. The threshold for pellet ELM triggering with 0.8×10^{20} D pellet injection with $v_p = 560$ m/s is between a pedestal pressure of $p_{e,ped} = 5.6$ and 5.8 kPa according to Figure 4 and Table 1.

To assess the impact of the pellet size on the simulated lag-time, also pellets with 0.4×10^{20} D atoms and 1.5×10^{20} D atoms were studied. The small pellet size is below the sizes experimentally accessible in ASDEX Upgrade, and the large pellet size corresponds approximately to the upper limit of pellet sizes experimentally accessible. With the small pellet, no ELM triggering was observed up to time point 12 ms, i.e., the small pellet never triggers an ELM in this work. The large pellet injection shows a transition between no-ELM response and ELM-triggering between injections at 6 ms and 8 ms which corresponds to $p_{e,ped} = 4.8$ kPa and 5.25 kPa. Thus, we observe a dependency of the lag-time on the injected pellet size. All pellet-triggered ELMs correspond to a crash of the pedestal profiles within ~ 0.4 ms, independent of the pellet size or pellet injection time. A pronounced difference in the toroidal mode spectrum was observed in the simulations. In no-ELM response cases, the spectrum is a lot narrower than in the ELM-triggering cases, while the $n = 1$ component directly induced by the pellet is dominant in all cases.

The pellet-triggered ELM cases show a pronounced toroidal asymmetry of the heat deposition consistent with simulations of DIII-D [24] and JET [29], where self-consistent

plasma flows and bootstrap current had not been taken into account. The heat deposition along the toroidal angle is observed to be largely independent from the pellet size which triggers the ELM crash. The footprint of the heat flux onto the divertor target is thus characterized by the magnetic field configuration, which is determined by the ELM crash itself. Similarities and differences between spontaneous and pellet-triggered ELM crashes are beyond the scope of this work and are separately studied in Ref. [32].

Finally, as a further important parameter, the dependence of the plasma dynamics onto the pellet injection velocity has been studied. JOREK modelling finds that it is typically easier to trigger an ELM when injecting the pellets faster (for the considered plasma and pellet sizes). Further investigations will be carried out in the future.

The dependence of the injection velocity of 1.5×10^{20} D pellets injected at 8 ms has been investigated for 560 m/s, 300 m/s and 240 m/s. In case of high speed injection velocity of the pellet, the magnetic energies show stronger growth with respect to the cases of slow injection velocity. This is due to the deeper penetration of the pellet in the plasma (the amplitude of the perturbation is larger for higher v_p). When the pellet injection is fast, the pellet rapidly reaches the inside of the pedestal where the plasma temperature is high. With the local high temperature, the pellet ablates quickly and creates a large density perturbation near the pedestal top, which excites the MHD modes causing the ELM crash. A velocity scan for a smaller pellet (0.8×10^{20} D atoms) injected at 14 ms shows that with an injection velocity 800 m/s, the pellet reaches to the flux surface of $q = 3$ and $q = 2$ ($\Psi_N \approx 0.72$ and 0.51 , respectively). This pellet reaching the core, does not only trigger an ELM crash, but also produces a large enough perturbation for giving rise to the growth of a $2/1$ neoclassical tearing mode at the $q = 2$ rational surface. The energy loss caused by pellet-triggered ELMs observes a non-monotonic dependency to the injection velocity (with all other pellet parameters kept constant). It is important to note that pellet size and velocity can typically not be modified independently in the experiment. Larger pellets are injected with lower velocities. Consequently, the two effects observed in our simulation would cancel to some extent in experiments: large pellets trigger easier, but the slower injection velocity acts in the opposite direction.

As already mentioned, the comparison of spontaneous and pellet-triggered plasmas is studied separately in detail in Ref. [32]. Further work will attempt to demonstrate pellet ELM pacing over several ELM cycles based on a simulation setup like described in Ref. [25] for spontaneous ELMs. Furthermore, pellet injection into ELM mitigated plasmas will be studied in the future to investigate the compatibility of fuelling pellets with ELM mitigation or suppression.

References

- [1] A. Loarte, G. Huijsmans, S. Futatani, L.R. Baylor, T.E. Evans, D. M. Orlov, O. Schmitz, M. Becoulet, P. Cahyna, Y. Gribov, A. Kavin, A. Sashala Naik, D.J. Campbell, T. Casper, E. Daly, H. Frerichs, A. Kischner, R. Laengner, S. Lisgo, R.A. Pitts, G. Saibene, and A. Wingen. Progress on the application of ELM control schemes to ITER scenarios from the non-active phase to DT operation. *Nuclear Fu-*

sion, 54(3):033007, 2014. URL <https://iopscience.iop.org/article/10.1088/0029-5515/54/3/033007/meta>.

- [2] T.E. Evans, M.E. Fenstermacher, R.A. Moyer, T.H. Osborne, J.G. Watkins, P. Gohil, I. Joseph, M.J. Schaffer, L.R. Baylor, M. Bécoulet, J.A. Boedo, K.H. Burrell, J.S. deGrassie, K.H. Finken, T. Jernigan, M.W. Jakubowski, C.J. Lasnier, M. Lehnen, A.W. Leonard, J. Lonnroth, E. Nardon, V. Parail, O. Schmitz, B. Unterberg, and W.P. West. Rmp ELM suppression in diii-d plasmas with iter similar shapes and collisionalities. *Nuclear Fusion*, 48(2):024002, 2008. URL <http://stacks.iop.org/0029-5515/48/i=2/a=024002>.
- [3] P.T. Lang, G.D. Conway, T. Eich, L. Fattorini, O. Gruber, S. Günter, L.D. Horton, S. Kalvin, A. Kallenbach, M. Kaufmann, G. Kocsis, A. Lorenz, M.E. Manso, M. Maraschek, V. Mertens, J. Neuhauser, I. Nunes, W. Schneider, W. Suttrop, H. Urano, and the ASDEX Upgrade Team. ELM pace making and mitigation by pellet injection in ASDEX Upgrade. *Nuclear Fusion*, 44(5):665, 2004. URL <https://iopscience.iop.org/article/10.1088/0029-5515/44/5/010/meta>.
- [4] P.T. Lang, J. Neuhauser, L.D. Horton, T. Eich, L. Fattorini, J.C. Fuchs, O. Gehre, A. Herrmann, P. Ignacz, M. Jakobi, S. Kalvin, M. Kaufmann, G. Kocsis, B. Kurzan, C. Maggi, M.E. Manso, M. Maraschek, V. Mertens, A. Muck, H.D. Murmann, R. Neu, I. Nunes, D. Reich, M. Reich, S. Saarelma, W. Sandmann, J. Stober, U. Vogl, , and the ASDEX Upgrade Team. ELM frequency control by continuous small pellet injection in asdex upgrade. *Nuclear Fusion*, 43(10):1110, 2003. URL <https://iopscience.iop.org/article/10.1088/0029-5515/43/10/012>.
- [5] L. R. Baylor, N. Commaux, T. C. Jernigan, S. J. Meitner, S. K. Combs, R. C. Isler, E. A. Unterberg, N. H. Brooks, T. E. Evans, A. W. Leonard, T. H. Osborne, P. B. Parks, P. B. Snyder, E. J. Strait, M. E. Fenstermacher, C. J. Lasnier, R. A. Moyer, A. Loarte, G. T. A. Huijsmans, , and S. Futatani. Reduction of edge localized mode intensity on DIII-D by on-demand triggering with high frequency pellet injection and implications for ITER. *Physics of Plasmas*, 20(8):082513, 2013. URL <https://aip.scitation.org/doi/10.1063/1.4818772>.
- [6] P.T. Lang, A. Burckhart, M. Bernert, L. Casali, R. Fischer, O. Kardaun, G. Kocsis, M. Maraschek, A. Mlynek, B. Plöckl, M. Reich, F. Ryter, J. Schweinzer, B. Sieglin, W. Suttrop, T. Szepesi, G. Tardini, E. Wolfrum, D. Zasche, and H. Zohm and. ELM pacing and high-density operation using pellet injection in the ASDEX upgrade all-metal-wall tokamak. *Nuclear Fusion*, 54(8):083009, jun 2014. doi:10.1088/0029-5515/54/8/083009. URL <https://doi.org/10.1088/0029-5515/54/8/083009>.
- [7] A. Herrmann (Guest editor). Special Issue on ASDEX Upgrade. *Fusion Science and Technology*, 44:1–747, 2003.
- [8] P.T. Lang, B. Alper, R. Buttery, K. Gal, J. Hobirk, J. Neuhauser, M. Stamp, and JET-EFDA contributors. ELM triggering by local pellet perturbations in type-I

-
- ELMy H-mode plasma at JET. *Nuclear Fusion*, 47(8):754, 2007. URL <https://iopscience.iop.org/article/10.1088/0029-5515/47/8/005/pdf>.
- [9] P T Lang, K Gal, J Hobirk, S Kalvin, G Kocsis, V Mertens, J Neuhauser, M Maraschek, W Suttrop, G Veres, and the ASDEX Upgrade Team. Investigations on the ELM cycle by local 3D perturbation experiments. *Plasma Physics and Controlled Fusion*, 48(5A):A141, 2006. URL <https://iopscience.iop.org/article/10.1088/0741-3335/48/5A/S13/pdf>.
 - [10] L. R. Baylor, N. Commaux, T. C. Jernigan, N. H. Brooks, S. K. Combs, T. E. Evans, M. E. Fenstermacher, R. C. Isler, C. J. Lasnier, S. J. Meitner, R. A. Moyer, T. H. Osborne, P. B. Parks, P. B. Snyder, E. J. Strait, E. A. Unterberg, , and A. Loarte. Reduction of edge-localized mode intensity using high-repetition-rate pellet injection in tokamak H-Mode plasmas. *Physical Review Letters*, 110:245001, 2013. URL <https://doi.org/10.1103/PhysRevLett.110.245001>.
 - [11] F. Romanelli, R. Kamendje, and on behalf of JET-EFDA Contributors. Overview of JET results. *Nuclear Fusion*, 49(10):104006, 2009. URL <https://iopscience.iop.org/article/10.1088/0029-5515/49/10/104006/meta>.
 - [12] G. Kocsis, S. Kálvin, P.T. Lang, M. Maraschek, J. Neuhauser, W. Schneider, T. Szepesi, and the ASDEX Upgrade Team. Spatio-temporal investigations on the triggering of pellet induced ELMs. *Nuclear Fusion*, 47(9):1166, 2007. URL <https://iopscience.iop.org/article/10.1088/0029-5515/47/9/013/pdf>.
 - [13] P.T. Lang, K. Lackner, M. Maraschek, B. Alper, E. Belonohy, K. Gál, J. Hobirk, A. Kallenbach, S. Kálvin, G. Kocsis, C.P. Perez von Thun, W. Suttrop, T. Szepesi, R. Wenninger, H. Zohm, the ASDEX Upgrade Team, and JET-EFDA contributors. Investigation of pellet-triggered MHD events in ASDEX Upgrade and JET. *Nuclear Fusion*, 48(9):095007, 2008. URL <http://stacks.iop.org/0029-5515/48/i=9/a=095007>.
 - [14] P T Lang, H Meyer, G Birkenmeier, A Burckhart, I S Carvalho, E Delabie, L Frassinetti, G Huijsmans, A Loarte G Kocsi and, C F Maggi, M Maraschek, B Ploekl, F Rimini, F Ryter, S Saarelma, T Szepesi, E Wolfrum, ASDEX Upgrade Team, and JET Contributors. ELM control at the L-H transition by means of pellet pacing in the asdex upgrade and JET all-metal-wall tokamaks. *Plasma Physics and Controlled Fusion*, 57(4):045011, 2015. URL <https://iopscience.iop.org/article/10.1088/0741-3335/57/4/045011/meta>.
 - [15] C.R. Sovinec, A.H. Glasser, T.A. Gianakon, D.C. Barnes, R.A. Nebel, S.E. Kruger, S.J. Plimpton, A. Tarditi, M.S. Chu, and the NIMROD Team. Nonlinear magnetohydrodynamics with high-order finite elements. *J. Comp. Phys.*, 195:355, 2004.
 - [16] N. M. Ferraro, S. C. Jardin, and P. B. Snyder. Ideal and resistive edge stability calculations with m3d-c1. *Physics of Plasmas*, 17:102508, 2010.

-
- [17] B.D. Dudson, M.V. Umansky, X.Q. Xu, P.B. Snyder, and H.R. Wilson. Bout++: A framework for parallel plasma fluid simulations. *Computer Physics Communications*, 180(9):1467 – 1480, 2009. ISSN 0010-4655. doi:10.1016/j.cpc.2009.03.008.
- [18] G.T.A. Huysmans and O. Czarny. MHD stability in x-point geometry: simulation of ELMs. *Nuclear Fusion*, 47(7):659, 2007. doi:10.1088/0029-5515/47/7/016.
- [19] M. Bécoulet, F. Orain, G. T. A. Huijsmans, S. Pamela, P. Cahyna, M. Hoelzl, X. Garbet, E. Franck, E. Sonnendrücker, G. Dif-Pradalier, C. Passeron, G. Latu, J. Morales, E. Nardon, A. Fil, B. Nkonga, A. Ratnani, and V. Grandgirard. Mechanism of edge localized mode mitigation by resonant magnetic perturbations. *Phys. Rev. Lett.*, 113:115001, Sep 2014. doi:10.1103/PhysRevLett.113.115001.
- [20] M. Hoelzl, D. Hu, E. Nardon, and G. T. A. Huijsmans. First predictive simulations for deuterium shattered pellet injection in ASDEX Upgrade. *Physics of Plasmas*, 27(2):022510, 2020. doi:10.1063/1.5133099.
- [21] F. Orain, M. Bécoulet, G. Dif-Pradalier, G. Huijsmans, S. Pamela, E. Nardon, C. Passeron, G. Latu, V. Grandgirard, A. Fil, A. Ratnani, I. Chapman, A. Kirk, A. Thornton, M. Hoelzl, and P. Cahyna. Non-linear magnetohydrodynamic modeling of plasma response to resonant magnetic perturbations. *Physics of Plasmas*, 20(10):102510, 2013. doi:10.1063/1.4824820.
- [22] F.J. Artola, G.T.A. Huijsmans, M. Hoelzl, P. Beyer, A. Loarte, and Y. Gribov. Non-linear magnetohydrodynamic simulations of edge localised mode triggering via vertical position oscillations in ITER. *Nuclear Fusion*, 58(9):096018, jul 2018. doi:10.1088/1741-4326/aace0e.
- [23] F. Liu, G.T.A. Huijsmans, A. Loarte, A.M. Garofalo, W.M. Solomon, P.B. Snyder, M. Hoelzl, and L. Zeng. Nonlinear MHD simulations of Quiescent H-mode plasmas in DIII-D. *Nuclear Fusion*, 55(11):113002, 2015. URL <http://stacks.iop.org/0029-5515/55/i=11/a=113002>.
- [24] S. Futatani, G. Huijsmans, A. Loarte, L.R. Baylor, N. Commaux, T.C. Jernigan, M.E. Fenstermacher, C. Lasnier, T.H. Osborne, and B. Pegourié. Non-linear MHD modelling of ELM triggering by pellet injection in DIII-D and implications for ITER. *Nuclear Fusion*, 54(7):073008, 2014. URL <http://stacks.iop.org/0029-5515/54/i=7/a=073008>.
- [25] A Cathey, M Hoelzl, and et al XXX. Simulations of multiple type-I ELM cycles in ASDEX Upgrade. *Nuclear Fusion*, XXX(XXX):submitted, 2020. doi:XXX.
- [26] S.J. Diem, L.R. Baylor, N.M. Ferraro, B.C. Lyons, D. Shiraki, and R.S. Wilcox. Utilizing m3d-c1 to understand triggering of elms in pellet pacing experiments in diii-d iter-like plasmas. *Proceedings of the 46th EPS Conference on Plasma Physics*, page P1.1055, 2019.

-
- [27] A. Fil, E. Kolemen, A. Bortolon, N. Ferraro, S. Jardin, P. B. Parks, R. Lunsford, and R. Maingi. Modeling of lithium granule injection in nstx with m3d-c1. *Nuclear Materials and Energy*, 12:1094, 2017. URL <https://www.sciencedirect.com/science/article/pii/S2352179116302708#bib0001>.
- [28] G. T. A. Huysmans, S. Pamela, E. van der Plas, and P. Ramet. Non-linear MHD simulations of edge localized modes (ELMs). *Plasma Physics and Controlled Fusion*, 51(12):124012, 2009. URL <http://stacks.iop.org/0741-3335/51/i=12/a=124012>.
- [29] S. Futatani, S. Pamela, L. Garzotti, G. T. A. Huijsmans, M. Hoelzl, D. Frigione, M. Lennholm, and and. Non-linear magnetohydrodynamic simulations of pellet triggered edge-localized modes in JET. *Nuclear Fusion*, 60(2):026003, dec 2019. doi:10.1088/1741-4326/ab56c7.
- [30] D. Frigione, L. Garzotti, M. Lennholm, B. Alper, G. Artaserse, P. Bennett, E. Giovannozzi, T. Eich, G. Kocsis, P. T. Lang, G. Maddaluno, R. Mooney, M. Rack, G. Sips, G. Tvalashvili, B. Viola, D. Wilkes, and JET-EFDA Contributors. Diver-tor load footprint of ELMs in pellet triggering and pacing experiments at JET. *Journal of Nuclear Materials*, 463:714, 2015. URL <https://www.sciencedirect.com/science/article/abs/pii/S002231151500063X>.
- [31] R. P. Wenninger, T. H. Eich, G. T. A. Huysmans, P. T. Lang, S. Devaux, S. Jachmich, F. Köchl, and JET EFDA Contributors. Scrape-off layer heat transport and diver-tor power deposition of pellet-induced edge localized modes. *Plasma Physics and Controlled Fusion*, 53(10):105002, aug 2011. doi:10.1088/0741-3335/53/10/105002.
- [32] A. Cathey, S. Futatani, M. Hoelzl, and et al XXX. Comparing natural and pel-let triggered elms via non-linear extended mhd simulations. *Plasma Physics and Controlled Fusion*, XXX(XXX):in preparation, 2020. doi:XXX.
- [33] H. Meyer, C. Angioni, C. G. Albert, N. Arden, R. Arredondo Parra, O. Asunta, M. de Baar, M. Balden, V. Bandaru, K. Behler, A. Bergmann, J. Bernardo, M. Bern-ert, A. Biancalani, R. Bilato, G. Birkenmeier, T. C. Blanken, V. Bobkov, A. Bock, T. Bolzonella, A. Bortolon, B. Böswirth, C. Bottereau, A. Bottino, H. van den Brand, S. Brezinsek, D. Brida, F. Brochard, C. Bruhn, J. Buchanan, A. Buh-ler, A. Burckhart, Y. Camenen, D. Carlton, M. Carr, D. Carralero, C. Castaldo, M. Cavedon, C. Cazzaniga, S. Ceccuzzi, C. Challis, A. Chankin, S. Chapman, C. Cianfarani, F. Clairet, S. Coda, R. Coelho, J. W. Coenen, L. Colas, G. D. Con-way, S. Costea, D. P. Coster, T. B. Cote, A. Creely, G. Croci, G. Cseh, A. Czarnecka, I. Cziegler, O. D’Arcangelo, P. David, C. Day, R. Delogu, P. de Marné, S. S. Denk, P. Denner, M. Dibon, A. Di Siena, D. Douai, A. Drenik, R. Drube, M. Dunne, B. P. Duval, R. Dux, T. Eich, S. Elgeti, K. Engelhardt, B. Erdös, I. Erofeev, B. Es-posito, E. Fable, M. Faitsch, U. Fantz, H. Faugel, I. Faust, F. Felici, J. Ferreira, S. Fietz, A. Figueredo, R. Fischer, O. Ford, L. Frassinetti, S. Freethy, M. Fröschle, G. Fuchert, J. C. Fuchs, H. Fünfgelder, K. Galazka, J. Galdon-Quiroga, A. Gallo,

Y. Gao, S. Garavaglia, A. Garcia-Carrasco, M. Garcia-Muñoz, B. Geiger, L. Giannone, L. Gil, E. Giovannozzi, C. Gleason-González, S. Glöggler, M. Gobbin, T. Görler, I. Gomez Ortiz, J. Gonzalez Martin, T. Goodman, G. Gorini, D. Gradic, A. Gräter, G. Granucci, H. Greuner, M. Griener, M. Groth, A. Gude, S. Günter, L. Guimaraes, G. Haas, A.H. Hakola, C. Ham, T. Happel, N. den Harder, G.F. Harrer, J. Harrison, V. Hauer, T. Hayward-Schneider, C.C. Hegna, B. Heine-mann, S. Heinzl, T. Hellsten, S. Henderson, P. Hennequin, A. Herrmann, M.F. Heyn, E. Heyn, F. Hitzler, J. Hobirk, K. Höfler, M. Hölzl, T. Höschen, J.H. Holm, C. Hopf, W.A. Hornsby, L. Horvath, A. Houben, A. Huber, V. Igochine, T. Ilkei, I. Ivanova-Stanik, W. Jacob, A.S. Jacobsen, F. Janky, A. Jansen van Vuuren, A. Jardin, F. Jaulmes, F. Jenko, T. Jensen, E. Joffrin, C.-P. Käsemann, A. Kallenbach, S. Kálvin, M. Kantor, A. Kappatou, O. Kardaun, J. Karhunen, S. Kasilov, Y. Kazakov, W. Kernbichler, A. Kirk, S. Kjer Hansen, V. Klevarova, G. Koc-sis, A. Köhn, M. Koubiti, K. Krieger, A. Krivska, A. Krämer-Flecken, O. Kud-lacek, T. Kurki-Suonio, B. Kurzan, B. Labit, K. Lackner, F. Laggner, P.T. Lang, P. Lauber, A. Lebschy, N. Leuthold, M. Li, O. Linder, B. Lipschultz, F. Liu, Y. Liu, A. Lohs, Z. Lu, T. Luda di Cortemiglia, N.C. Luhmann, R. Lunsford, T. Lunt, A. Lyssoivan, T. Maceina, J. Madsen, R. Maggiora, H. Maier, O. Maj, J. Mailloux, R. Maingi, E. Maljaars, P. Manas, A. Mancini, A. Manhard, M.-E. Manso, P. Man-tica, M. Mantsinen, P. Manz, M. Maraschek, C. Martens, P. Martin, L. Marrelli, A. Martitsch, M. Mayer, D. Mazon, P.J. McCarthy, R. McDermott, H. Meister, A. Medvedeva, R. Merkel, A. Merle, V. Mertens, D. Meshcheriakov, O. Meyer, J. Miettunen, D. Milanese, F. Mink, A. Mlynek, F. Monaco, C. Moon, F. Nabais, A. Nemes-Czopf, G. Neu, R. Neu, A.H. Nielsen, S.K. Nielsen, V. Nikolaeva, M. No-cente, J.-M. Noterdaeme, I. Novikau, S. Nowak, M. Oberkofler, M. Oberparleiter, R. Ochoukov, T. Odstřil, J. Olsen, F. Orain, F. Palermo, O. Pan, G. Papp, I. Pa-radela Perez, A. Pau, G. Pautasso, F. Penzel, P. Petersson, J. Pinzón Acosta, P. Pi-ovesan, C. Piron, R. Pitts, U. Plank, B. Plaum, B. Ploekl, V. Plyusnin, G. Pokol, E. Poli, L. Porte, S. Potzel, D. Prisiazhniuk, T. Pütterich, M. Ramisch, J. Ras-mussen, G.A. Rattá, S. Ratynskaia, G. Raupp, G.L. Ravera, D. Réfy, M. Reich, F. Reimold, D. Reiser, T. Ribeiro, J. Riesch, R. Riedl, D. Rittich, J.F. Rivero-Rodriguez, G. Rocchi, M. Rodriguez-Ramos, V. Rohde, A. Ross, M. Rott, M. Rubel, D. Ryan, F. Ryter, S. Saarelma, M. Salewski, A. Salmi, L. Sanchis-Sanchez, J. San-tos, O. Sauter, A. Scarabosio, G. Schall, K. Schmid, O. Schmitz, P.A. Schnei-der, R. Schrittwieser, M. Schubert, T. Schwarz-Selinger, J. Schweinzer, B. Scott, T. Sehmer, E. Seliunin, M. Sertoli, A. Shabbir, A. Shalpegin, L. Shao, S. Sharapov, G. Sias, M. Siccino, B. Sieglin, A. Sigalov, A. Silva, C. Silva, D. Silvagni, P. Si-mon, J. Simpson, E. Smigelskis, A. Snicker, C. Sommariva, C. Sozzi, M. Spolaore, A. Stegmeir, M. Stejner, J. Stober, U. Stroth, E. Strumberger, G. Suarez, H.-J. Sun, W. Suttrop, E. Sytova, T. Szepesi, B. Tál, T. Tala, G. Tardini, M. Tardocchi, M. Teschke, D. Terranova, W. Tierens, E. Thorén, D. Told, P. Talias, O. Tudisco, W. Treutterer, E. Trier, M. Tripský, M. Valisa, M. Valovic, B. Vanovac, D. van Vugt, S. Varoutis, G. Verdoolaege, N. Vianello, J. Vicente, T. Vierle, E. Viezzer, U. von Toussaint, D. Wagner, N. Wang, X. Wang, M. Weiland, A.E. White, S. Wiesen,

M. Willensdorfer, B. Wiringer, M. Wischmeier, R. Wolf, E. Wolfrum, L. Xiang, Q. Yang, Z. Yang, Q. Yu, R. Zagórski, I. Zammuto, W. Zhang, M. van Zeeland, T. Zehetbauer, M. Zilker, S. Zoletnik, and H. Zohm. Overview of physics studies on ASDEX Upgrade. *Nuclear Fusion*, 59(11):112014, jul 2019. doi:10.1088/1741-4326/ab18b8.

- [34] Olivier Czarny and Guido Huysmans. Bezier surfaces and finite elements for MHD simulations. *Journal of Computational Physics*, 227(16):7423 – 7445, 2008. ISSN 0021-9991. doi:10.1016/j.jcp.2008.04.001.

Acknowledgements

This work has been carried out within the framework of the EUROfusion Consortium and has received funding from the Euratom research and training program 2014-2018 and 2019-2020 under grant agreement No 633053. The views and opinions expressed herein do not necessarily reflect those of the European Commission. In particular, contributions by EUROfusion work packages Enabling Research (EnR) and Medium Size Tokamaks (MST) is acknowledged. The author thankfully acknowledges the computer resources of PRACE (Partnership for Advanced Computing in Europe) and RES (Spanish Supercomputing Network) at MareNostrum and the technical support provided by Barcelona Supercomputing Center, and the support from Marconi-Fusion, the High Performance Computer at the CINECA headquarters in Bologna (Italy) for its provision of supercomputer resources. The work of S.F. is supported by a Ramón y Cajal grant from the Spanish Ministry of Economy and Competitiveness (RYC-2014-15206).

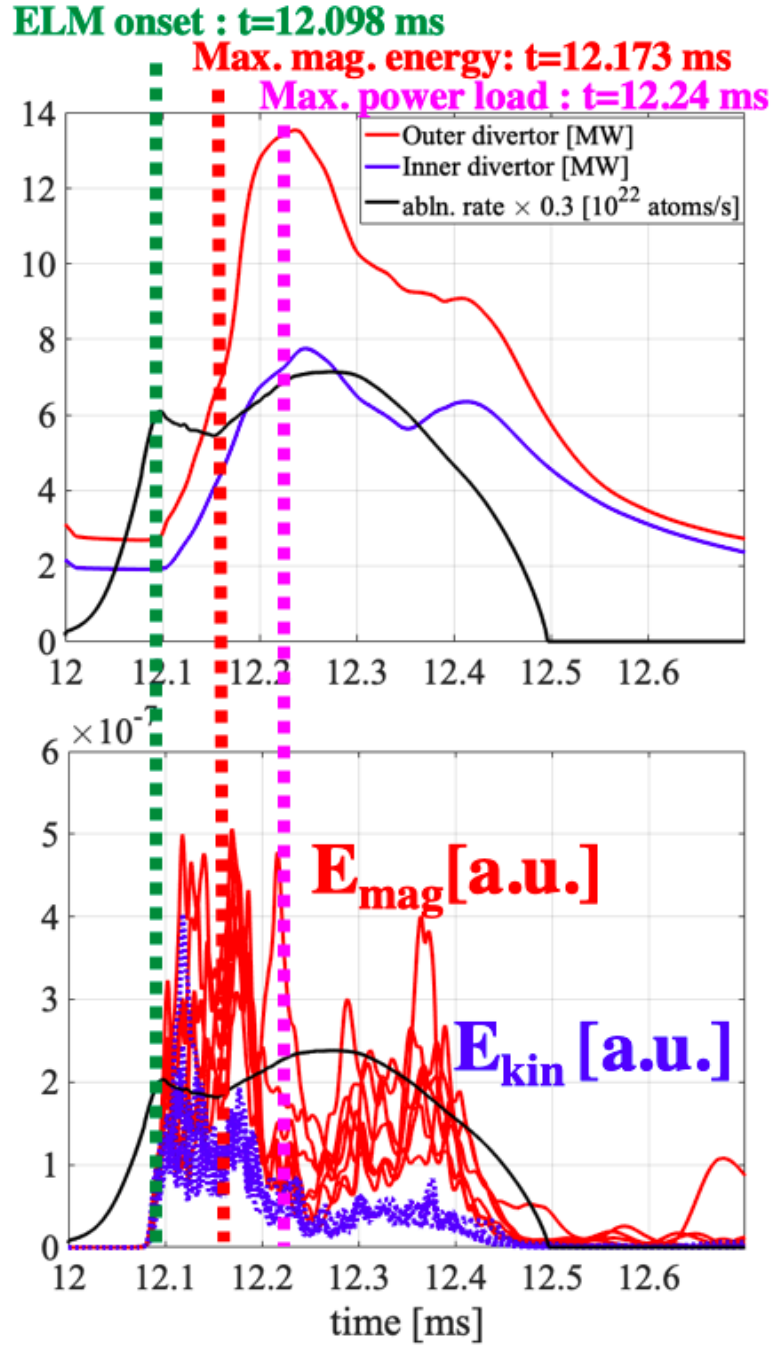


Figure 25: (Top panel) The time evolution of the power load onto the outer and the inner divertor target (plotted in red and blue lines, respectively). The time evolution of the ablation rate is plotted in black line. (Bottom panel) The time evolution of the magnetic energy (red lines) and the kinetic energy (blue lines) of high toroidal modes, $n = 6 \dots 12$.

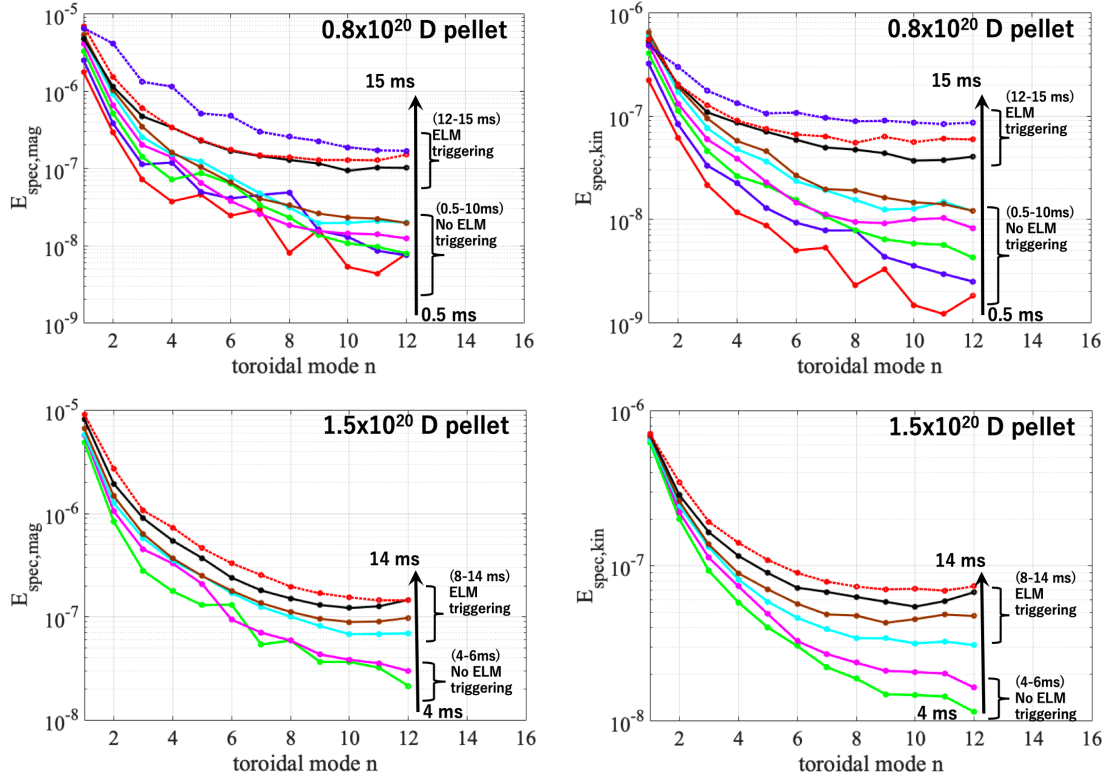


Figure 26: Time-averaged toroidal spectrum over the pellet ablation process. Left panel is the magnetic spectrum and right panel is the kinetic spectrum. Top panels show 0.8×10^{20} D pellet, bottom panels show 1.5×10^{20} D pellet.

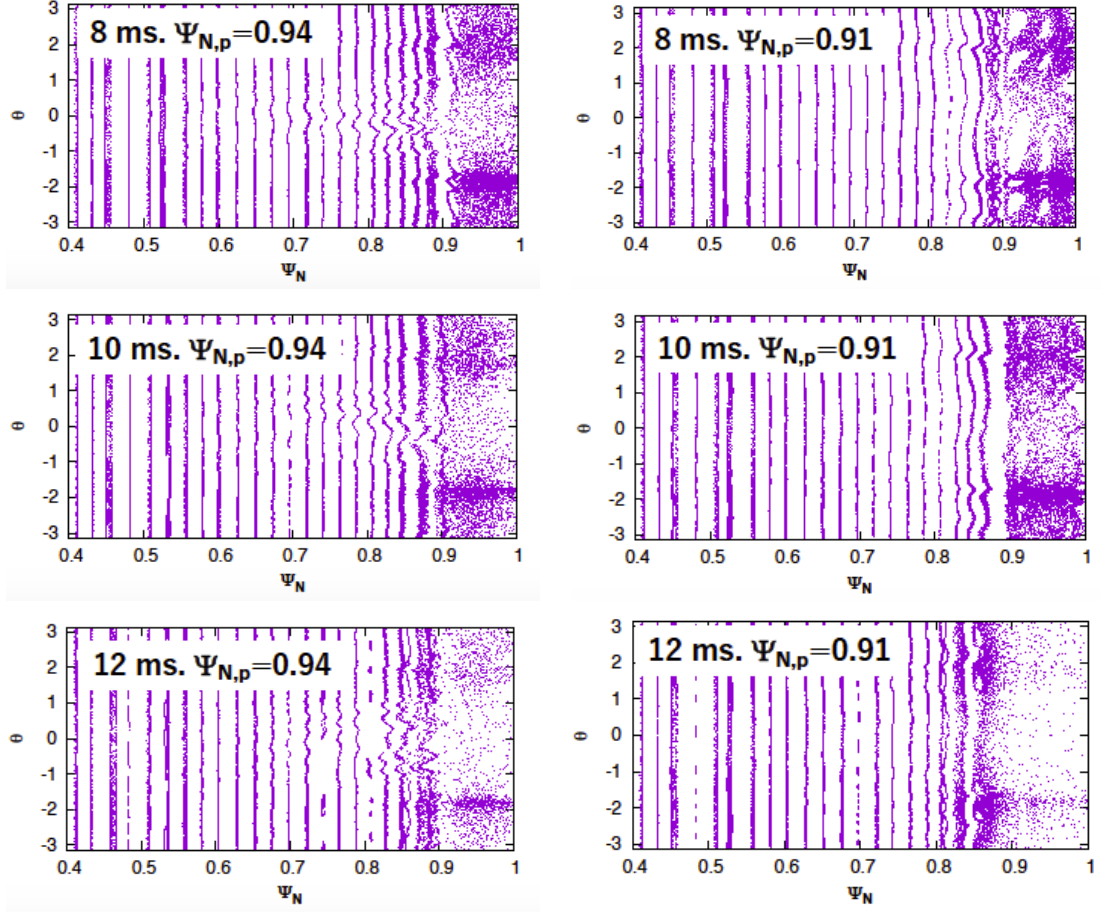


Figure 27: Poincaré plots for the pellet locations at $\Psi_{N,p} = 0.94$ and $\Psi_{N,p} = 0.91$, and for the injection times of $t_{\text{inj}} = 8\text{ms}$, 10 ms , and 12 ms .

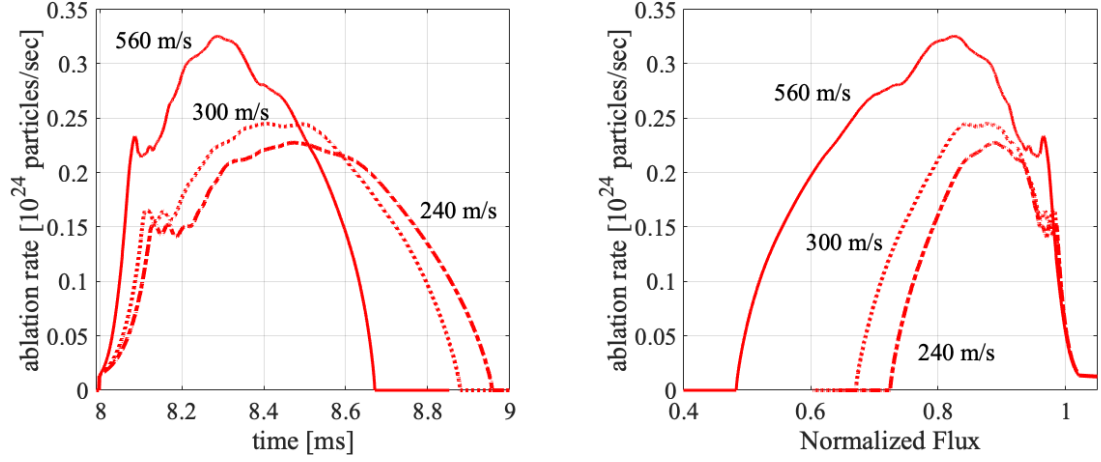


Figure 28: The pellet ablation rate versus time and the ablation rate profile versus normalized flux. The pellet size is $1.5 \times 10^{20} D$ injected at 8 ms for three injection velocity; 560 m/s (reference case), 300 m/s and 240 m/s.

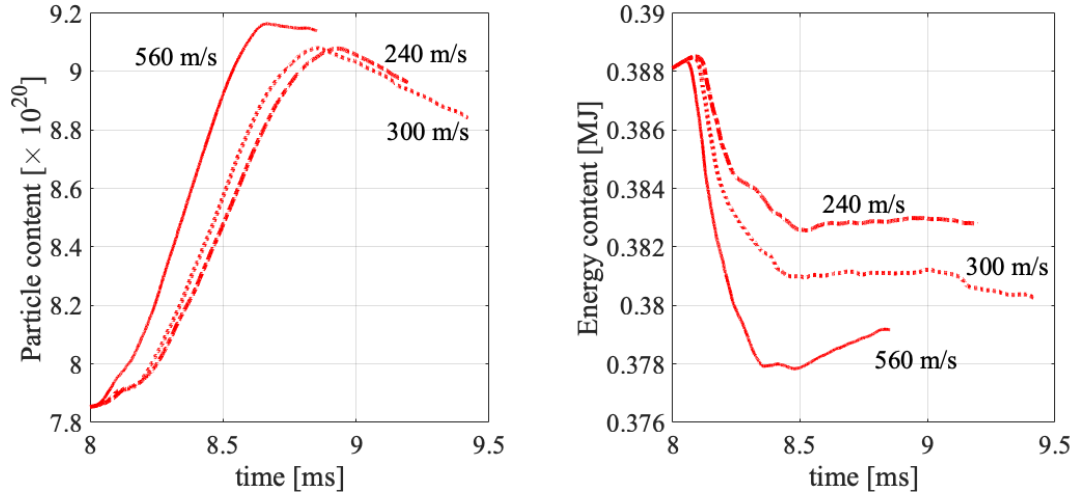


Figure 29: The particle and the energy content is plotted versus time. The pellet size is $1.5 \times 10^{20} D$ injected at 8 ms for three injection velocities; 560 m/s (reference case), 300 m/s and 240 m/s.

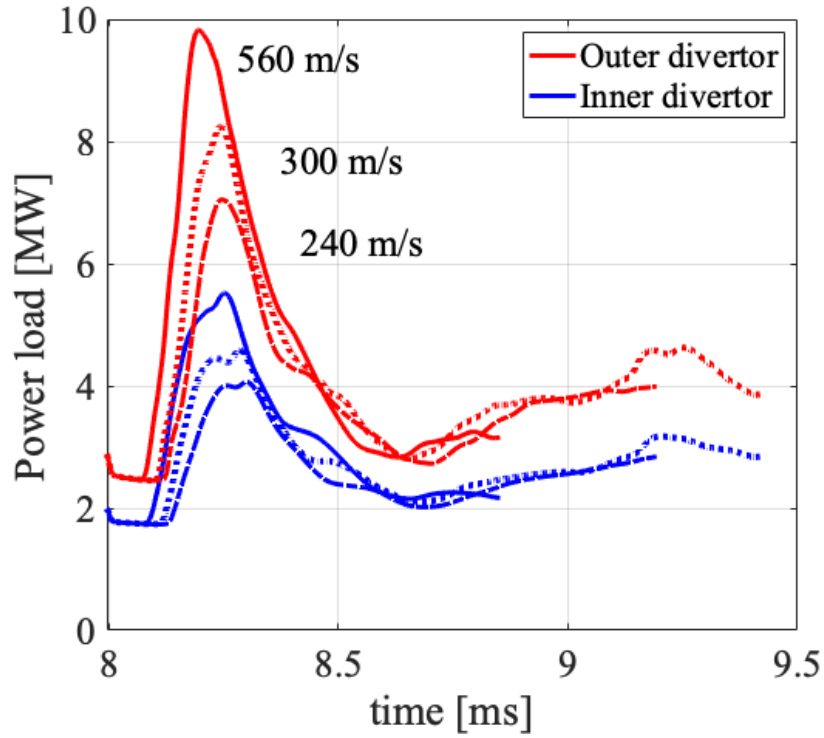


Figure 30: The time evolution of the power load onto the inner and the outer divertor targets which is caused by $1.5 \times 10^{20}D$ pellets injected at 8 ms, for 560 m/s (reference case), 300 m/s and 240 m/s.

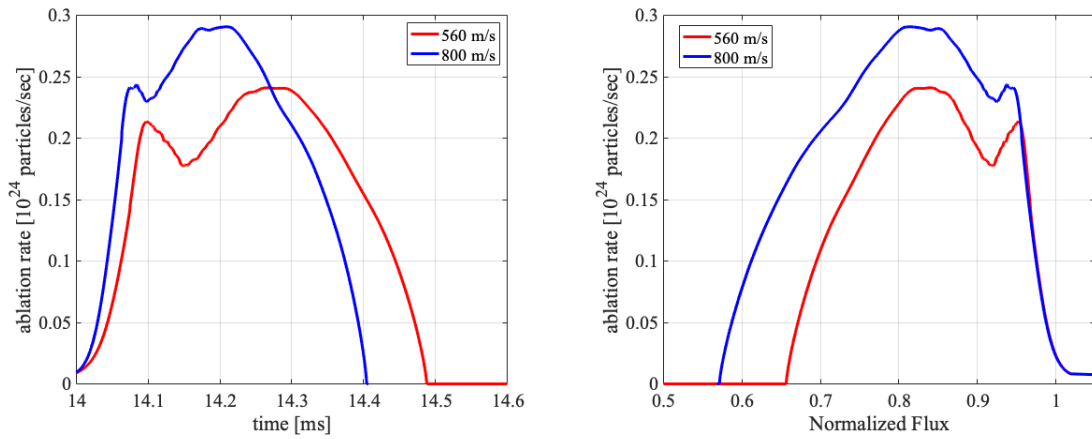


Figure 31: (Left panel) The time evolution of pellet ablation rate and (Right panel) the pellet ablation rate versus normalized flux. The pellet size is $0.8 \times 10^{20}D$ and the injection timing is 14 ms which triggers an ELM. Red lines are 560 m/s and blue lines are 800 m/s.

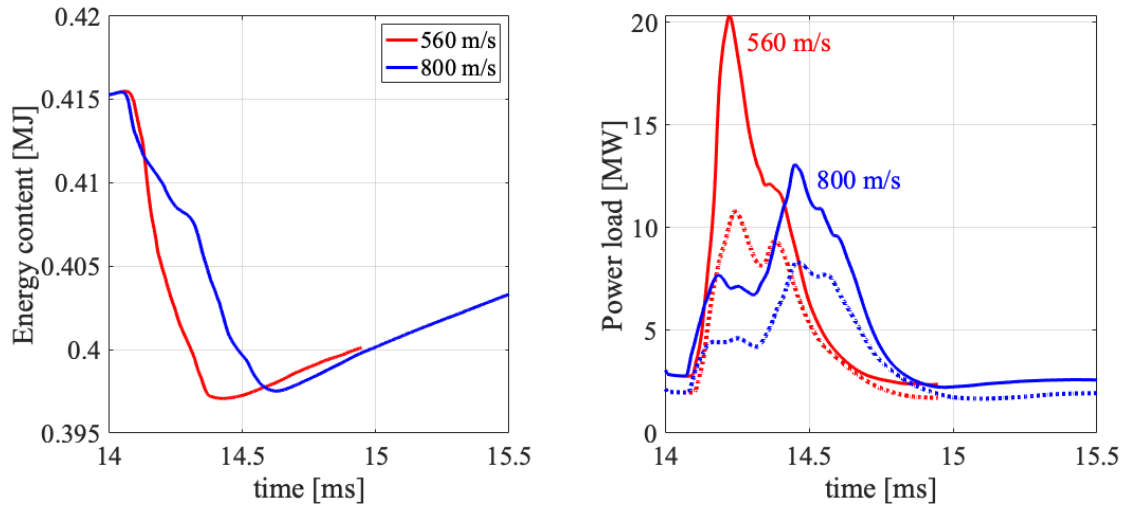


Figure 32: (Left panel) The time evolution of the energy content inside the separatrix for 560 m/s (reference injection speed) and 800 m/s. (Right panel) The time evolution of the power load onto the divertor targets. Solid and dashed lines are outer and inner divertor targets.

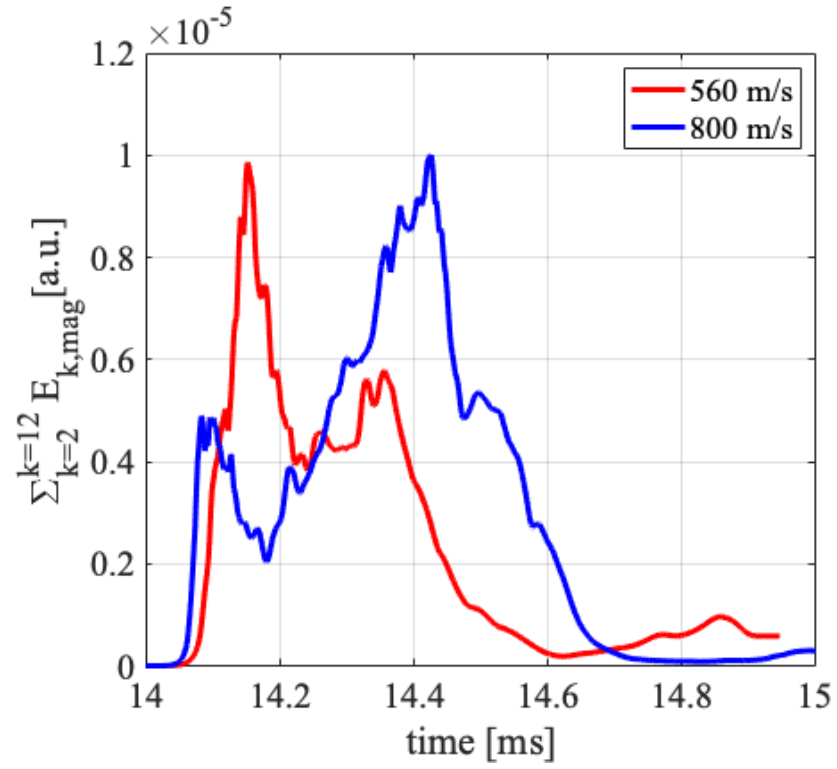


Figure 33: The time evolution of the integrated magnetic energies over $k = 2 - 12$, $\Sigma_{k=2}^{k=12} E_{k,\text{mag}}$, for 560 m/s pellet injection (reference case) and 800 m/s.

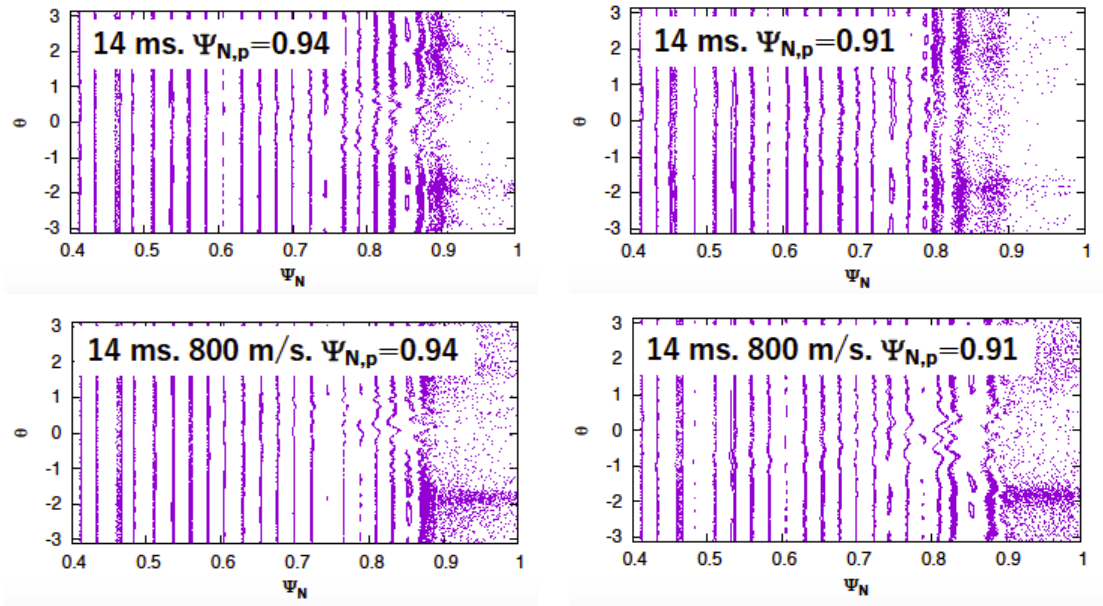


Figure 34: Poincaré plots for the pellet locations at $\Psi_{N,p} = 0.94$ and $\Psi_{N,p} = 0.91$, for the injection velocities of 560 m/s and 800 m/s.

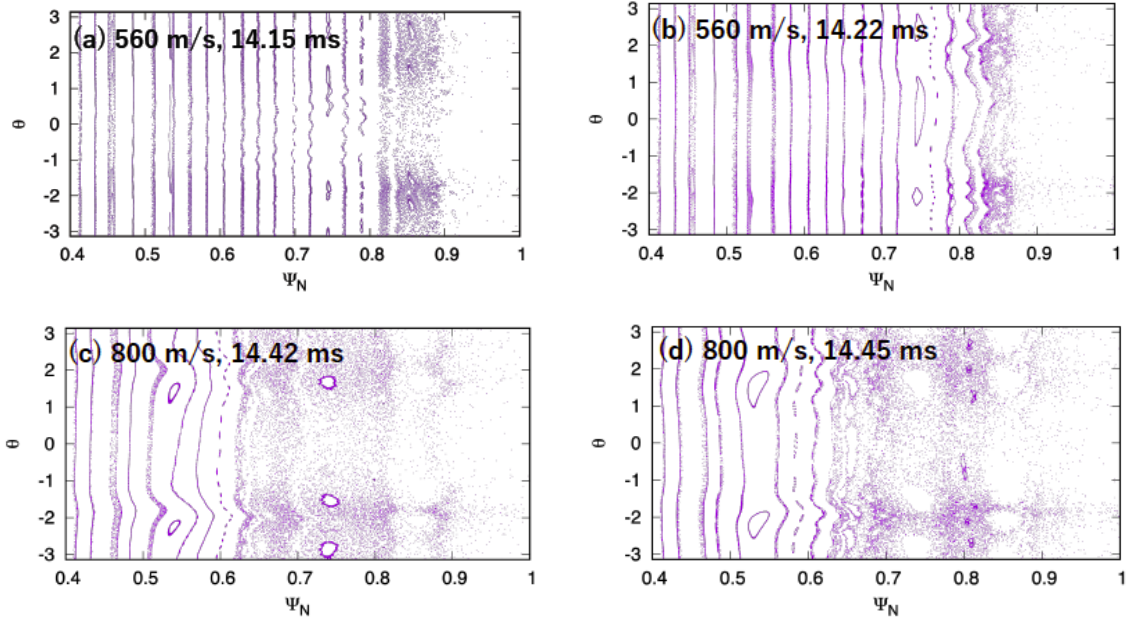


Figure 35: 0.8×10^{20} D pellet injection at 14 ms. (Left column) Poincare plot at the maximum magnetic energy $\sum_{k=2}^{k=12} E_{k,\text{mag}}$ for pellet injection speed of 560 m/s (14.15 ms) and 800 m/s (14.42 ms). (Right column) Poincare plot at the maximum power load onto the divertor target for pellet injection speed of 560 m/s (14.22 ms) and 800 m/s (14.45 ms).

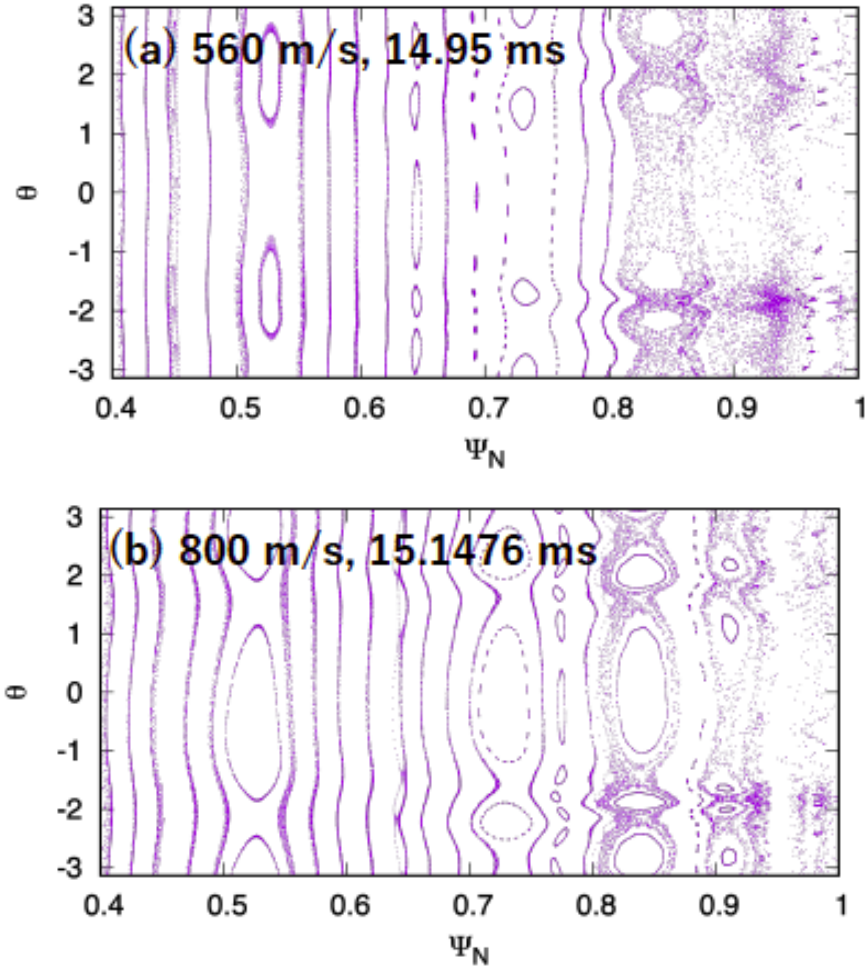


Figure 36: Poincaré plots during the relaxation state after the ELM crashes for the injection velocities of 560 m/s and 800 m/s. The times 14.95 ms (560 m/s) and 15.1476 ms (800 m/s) are plotted, which are 0.5 ms after the end of the thermal energy losses.